

Laboratory mid-IR spectra of equilibrated and igneous meteorites

Searching for observables of planetesimal debris

B.L. de Vries^{a,b,c}, H. Skogby^d, L.B.F.M. Waters^{e,f}, M. Min^{e,f}

^aStockholm University Astrobiology Centre, SE-106 91 Stockholm, Sweden

^bAlbaNova University Centre, Stockholm University, Department of Astronomy, SE-106 91 Stockholm, Sweden

^cScientific Support Office, Directorate of Science, European Space Research and Technology Centre (ESA/ESTEC), Keplerlaan 1, 2201 AZ Noordwijk, The Netherlands

^dDepartment of Geosciences, Swedish Museum of Natural History, Box 50007, SE-104 05 Stockholm, Sweden

^eSRON Netherlands Institute for Space Research, Sorbonnelaan 2, 3584 CA Utrecht, The Netherlands

^fAstronomical Institute Anton Pannekoek, University of Amsterdam, Science Park 904, 1098 XH, Amsterdam, The Netherlands

Abstract

Meteorites contain minerals from Solar System asteroids with different properties (like size, presence of water, core formation). We provide new mid-IR transmission spectra of powdered meteorites to obtain templates of how mid-IR spectra of asteroidal debris would look like. This is essential for interpreting mid-IR spectra of past and future space observatories, like the James Webb Space Telescope. First we present new transmission spectra of powdered ordinary chondrite, pallasite and HED meteorites and then we combine them with already available transmission spectra of chondrites in the literature, giving a total set of 64 transmission spectra. In detail we study the spectral features of minerals in these spectra to obtain measurables used to spectroscopically distinguish between meteorite groups. Being able to differentiate between dust from different meteorite types means we can probe properties of parent bodies, like their size, if they were wet or dry and if they are differentiated (core formation) or not.

We show that the transmission spectra of wet and dry chondrites, carbonaceous and ordinary chondrites and achondrite and chondrite meteorites are distinctly different in a way one can distinguish in astronomical mid-IR spectra. Carbonaceous chondrites type <3 (aqueously altered) show distinct features of hydrated silicates (hydrosilicates) compared to the olivine and pyroxene rich ordinary chondrites (dry and equilibrated meteorites). Also the iron concentration of the olivine in carbonaceous chondrites differs from ordinary chondrites, which can be probed by the wavelength peak position of the olivine spectral features. The transmission spectra of chondrites (not differentiated) are also strongly different from the achondrite HED meteorites (meteorites from differentiated bodies like 4 Vesta), where the latter show much stronger pyroxene signatures.

The two observables that spectroscopically separate the different meteorites groups (and thus the different types of parent bodies) are the pyroxene-olivine feature strength ratio and the peak shift of the olivine spectral features due to an increase in the iron concentration of the olivine.

Keywords: Meteorites, Mineralogy, Spectroscopy, Planetary formation, Debris disks

1. Introduction

Dust grains (micron-sized solid-state particles) play an essential role in many astrophysical environments. One of the prime examples is the formation and evolution of planets in proto-planetary disks. Small micron sized dust grains are the building blocks of planets. Proto-planetary disks are formed from interstellar dust and gas, where the lattice structure of the dust is amorphous and its composition is mostly silicate with some amounts of carbonaceous dust (Kemper et al., 2004; Min et al., 2007). In proto-planetary disks this dust can be annealed (the lattice structure is made crystalline due to heating) or it can be condensed from the gas (Tielens et al., 1998; Gail and Sedlmayr, 1999; Sogawa and Kozasa, 1999). Crystalline dust formation takes place in the inner parts of the disk. The crystals can subsequently be mixed with the outer parts of the disk (for example see Gail 2004).

The crystalline and amorphous dust in proto-planetary disks can be studied by observing their emission and absorption in the infrared. Much can be learned about the composition, grain size and grain temperature of the crystalline dust in proto-planetary disks by studying and modelling their spectral features (Waelkens et al., 1996; Meeus et al., 2001; Kessler-Silacci et al., 2006; Sturm et al., 2013; Maaskant et al., 2015). The wavelength position, strength and shape of the spectral features show that the crystalline olivine ($[\text{Mg,Fe}]_2\text{SiO}_4$) grains are very magnesium rich (at most the olivine has an $\text{Fe}/(\text{Mg}+\text{Fe})$ of $\sim 0.0-0.03$) and crystalline olivine is about 0-10 % (by mass) of the total dust content in the disk. Besides olivine, pyroxene ($[\text{Mg,Fe,Ca}]\text{SiO}_3$) is also detected in crystalline form (Juhász et al., 2010). Although more difficult to determine, the pyroxene seems to contain more iron than the olivine (for pyroxene Bowey et al. (2007); Sargent et al. (2009); Juhász et al. (2010) report $\text{Fe}/(\text{Mg}+\text{Fe})$ values of 10-25 %) and in some cases it can have an abundance equal to that of the crystalline olivine.

Email address: bldevries.science@gmail.com (B.L. de Vries)

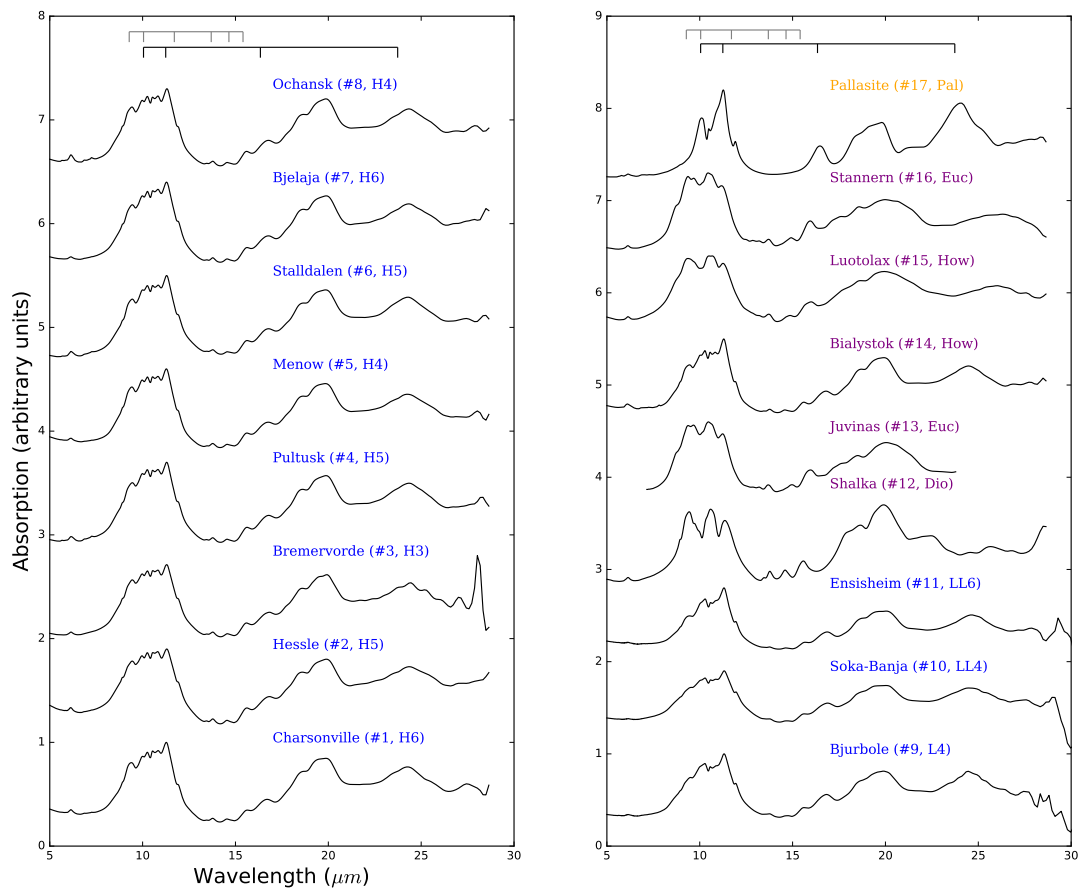


Figure 1: Absorbance infrared transmission spectra of the sample of meteorites presented in this work (see Tab. 1). The spectra are scaled and shifted. The ordinary chondrite names are shown in blue, the HED in purple and the pallasite in orange. The black and grey "forks" at the top indicate the olivine and pyroxene feature peak positions (respectively) of the features discussed in this work. The olivine and pyroxene cross-sections are plotted in Fig. 2.

Furthermore, Juhász et al. (2010) report that the pyroxene-olivine ratio decreases as a function of radius in the disk, which is difficult to explain based on equilibrium considerations (Gail, 2004).

In proto-planetary disks dust grains are used to form planetesimals and eventually planets. When the proto-planetary disk eventually sheds its gas and small dust grains a main-sequence star with a system of planetesimals and planets is left (Wyatt, 2008). During this evolution of the disk the minerals in the planetesimals and planets are influenced by parent-body processes. Depending on the properties and formation process of the parent-body these processes can be aqueous alteration, equilibration and melting due to heating (Hutchison, 2004). Relatively small planetesimals (several to a hundred of kilometers in diameter) can heat up several hundreds of Kelvin due to radiative decay of unstable elements (like ^{26}Al), during which diffusion between minerals can alter their composition (Kessel et al., 2007). Larger planetesimals (several hundreds of kilometers and up in diameter) and planets reach temperatures where the minerals melt and the body will differentiate (formation of a core and rocky crust), which has a strong influence on the composition and lattice structure of the minerals. An example of such a planetesimal in our Solar System is the asteroid 4 Vesta (Consolmagno and Drake, 1977; McCord et al., 1970).

The composition of planetesimals can be studied over astronomical distances by observing dynamically active systems where planetesimals have a high probability of colliding and being ground down to micron-sized dust grains (Wyatt, 2008). These micron-sized dust grains can form so called debris disks. It is important to note that the dust in these debris disks does not come from the proto-planetary disk, but consists of a second generation of dust coming from collisions in the system. Dust grains in debris disks can then be studied by analysing their infrared spectral features. Olofsson et al. (2012) studied young main-sequence stars with dust relatively close to the star at several hundreds of Kelvin (distances comparable to the asteroid belt). They found olivine with an iron content $\text{Fe}/(\text{Mg}+\text{Fe}) \sim 0.2$ and $\text{Py}/(\text{Ol}+\text{Py})$ ratios of 0.0-0.2, which compares well with Solar System asteroids (Nakamura et al., 2011). The dust produced in a Kuiper-belt like analogue in the system of the main-sequence star β Pictoris contains olivine that is very pure Mg-rich ($\text{Fe}/(\text{Mg}+\text{Fe})=0.01$) and no pyroxene is found (Chen et al., 2007; de Vries et al., 2012). The debris in the outskirts of β Pictoris compares best with cometary olivine found by for example the Stardust mission (Zolensky et al., 2008).

How minerals change due to parent-body processing can be understood from the meteoritic record of our Solar System. The minerals in meteorites can be studied in detail and they can be linked back to their parent-bodies and their properties. For example ordinary chondrites are linked to relatively small and equilibrated asteroids, some carbonaceous chondrites have been aqueously altered and have been linked to wet relatively small asteroids and the HED (howardite-eucrite-diogenite) achondrites are an example of achondrites linked to the differentiated asteroid 4 Vesta (for an overview see Hutchison 2004 and for the Dawn mission Russell et al. 2015). Considering the silicate minerals in meteorites, the dominant silicate in carbonaceous

chondrites with low metamorphic grade (type 1 and 2) are hydrated silicates (from here on hydrosilicates). Silicates in ordinary chondrites have experience little (type 3) to severe (type 4 and up) alteration due to heat which increased their pyroxene abundance and increased the iron content of their olivine and pyroxene minerals (up to $\text{Fe}/(\text{Mg}+\text{Fe}) \sim 0.16-0.32$ and $0.18-0.26$ respectively, Van Schmus 1969; Brearley and Jones 1998). The pyroxene content of achondrite meteorites is very high (>90 vol%) and besides pure pyroxene one also observes other phases like plagioclase (a solid-solution between albite ($\text{NaAlSi}_3\text{O}_8$) and anorthite ($\text{CaAl}_2\text{Si}_2\text{O}_8$), Hutchison 2004).

Besides detailed compositional information, much work has been done on reflectance and emission measurements (in the optical and near-IR, and both of surfaces and in powdered form, for an overview see for example Hutchison 2004). In this work we focus on transmission measurements of powdered meteoritic minerals in the mid-IR (5-25 μm). We focus on this method because it is directly comparable to observations of dust grains freed by parent body collisions in young planetary systems. This enables us to make a direct spectroscopic comparison between dust from Solar System asteroids and extra-solar planetesimals and thus learn about the properties and evolution of extra-solar planetesimals. Mid-IR spectra of powdered meteorites have been done by Morlok et al. (2010) (also see Morlok et al. 2012, 2014a,b), Beck et al. (2014) and Molster et al. (2003). Morlok et al. (2012) has studied mid-IR spectra of several powdered achondrites and Morlok et al. (2014b) of several powdered chondritic meteorites. Beck et al. (2014) measured the mid-IR spectra of powdered carbonaceous chondrites. Mid-IR spectra of an interplanetary dust particles (IPD) and micrometeorites have been presented in, for example, Sandford and Walker (1985); Molster et al. (2003); Bradley et al. (1999).

The goal of this work is to 1) complement the available sets of mid-IR spectra of powdered meteorites with missing chondritic and achondritic powdered meteorite spectra, 2) present an overview of the spectral properties of all powdered meteoritic mid-IR spectra that are available to date and study their differences and 3) define several quantitative measurements useful for determining the parent-body properties based on the dust and debris in astronomical environments. The first quantitative measurement on the spectra that we consider in this paper is the relative strengths of the pyroxene and olivine bands as an indication of the pyroxene-over-olivine ratio in the meteorite. The second measurement is the shift in peak position of several olivine and pyroxene spectral features since these shifts are indicative of the iron content of these silicates (Koike et al., 2003).

The paper is structured in such a way that we first introduce the measurements, sample selection and methods, followed by a presentation of the resulting spectra. Then we explain how we measure the wavelength peak positions of several olivine and pyroxene spectral features as well as the strength of several of these spectral features. This is followed by our results and we end with a discussion and conclusions.

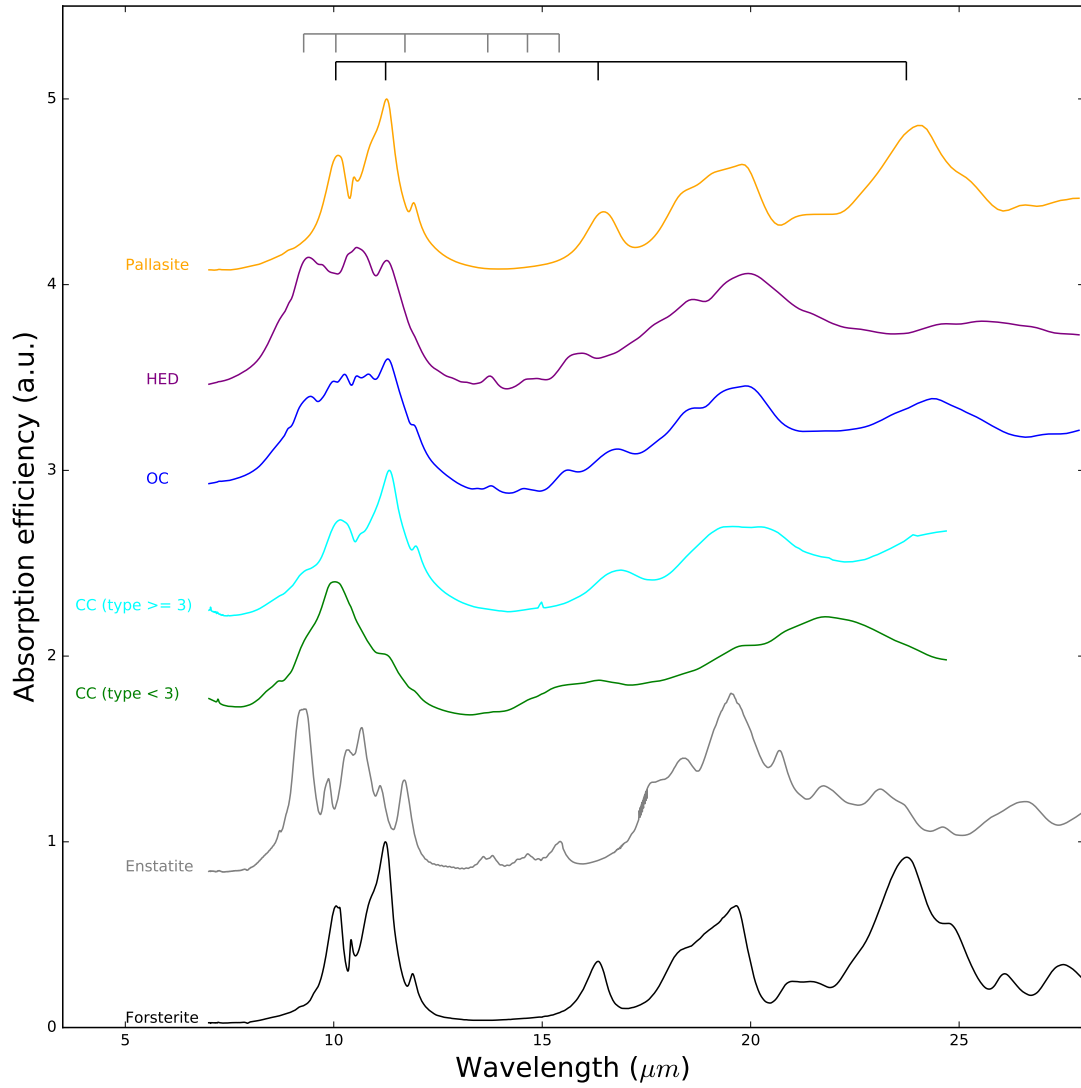


Figure 2: Averaged spectra for the carbonaceous chondrites with metamorphic grade lower than 3 (green), carbonaceous chondrites with type equal and larger than 3 (cyan), ordinary chondrites (blue), HED achondrites (purple) and a pallasite (orange). The "forks" at the top of the plot indicate the wavelength peak positions of pure Mg-rich olivine (black) and pure Mg-rich pyroxene bands (grey) discussed in this work. The opacities of synthetic Mg-rich olivine and Mg-rich pyroxene are shown at the bottom of the plot in black and grey respectively. All spectra are scaled and shifted. The carbonaceous chondrites are from Beck et al. (2014) and for a comparison with hydrosilicate spectra, please see their work.

Table 1: Meteorite sample of this work

Name	Type	Museum catalogue number
Charsonville	H6	NRM#65:0088
Hessle	H5	NRM#69:0402
Bremervörde	H3	NRM#57:0095
Pultusk	H5	NRM#77:0283
Menow	H4	NRM#LK7805
Ställdalen	H5	NRM#76:0347
Bjelaja Zerkov	H6	NRM#65:0108
Ochansk	H4	NRM#93:121
Bjurböle	L4	NRM#99:0420
Soko-Banja	LL4	NRM#884239
Ensisheim	LL6	NRM#600069
Shalka	diogenite	NRM#68:517
Juvinas	euclite	NRM#94:0099
Bialystok	euclite	NRM#86:0136
Luotolax	howardit	NRM#69:0664
Stannern	euclite	NRM#78:0134
Seymchan	pallasite	-

2. Measurements

2.1. Sample selection

For this study we focussed on meteorites that represent minerals and rocks in medium to large sized planetesimals (ten to hundreds of kilometres in diameter). Measurements of carbonaceous chondrites (Beck et al., 2014) and some ordinary chondrites (OC) (Morlok et al., 2010, 2012, 2014a) have been published, but in the literature the OC and HED groups are not completely sampled and the pallasite meteorite group is not measured. These are the meteorites for which we present mid-IR spectra in this work. We collected 13 samples from the meteorite collection of the Swedish Museum of Natural History, Stockholm. Our sample (see table 1) consists of 8 H-type OC (ranging from metamorphic grade 3 to 6), one L4 OC and an LL4 and LL6 OC. We also included 6 achondrites to the sample of which five HED and one pallasite. Among the HED we have one howardite, one diogenite and three euclites.

Later in this work we will combine the spectra we measured with spectra available in the literature. These are carbonaceous chondrites from Beck et al. (2014) and some spectra from Morlok et al. (2012, 2014a,b). We will also compare the meteorite spectra with synthetic laboratory measurements of several minerals. All these measurements and their numbers used in the upcoming plots are listed in tables 3 to 5.

2.2. Mid-IR spectra measurement technique

For the whole sample we obtained Fourier transform infrared (FTIR) transmission spectra in the mid-IR. For the FTIR we needed ~ 1 mg of sample material. This material was scraped from the meteorite using a diamond top drill and subsequently ground down in an agate mortar for several minutes. Some of the meteorite samples contained metallic iron grains which

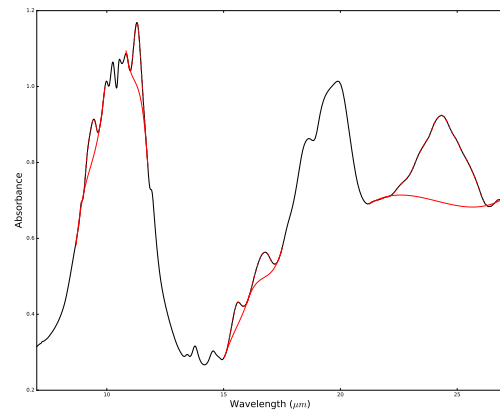


Figure 3: Example of the constructed continua (solid red line) and feature splines (dashed red line) for the case of the spectrum of Bjelaja Zerkov.

were removed using a magnet during the grinding process. Metallic iron does not have any spectral features and its absorption in the mid-IR is a smooth continuum (for example see Ordal et al. 1988). Therefore the removal of metallic iron has no impact on our results since we focus on spectral features and not on the continuum absorption.

The material was then mixed with 200-300 mgr of KBr and pressed into a pellet. A transmission spectrum in the 5-25 μm range is then obtained using a FTIR spectrometer (Bruker Equinox 55 and Vertex 70). The resulting spectra in absorbance mode are shown in Fig. 1.

Observational studies of dust freed from planetesimals in debris disks sample the bulk of the minerals freed from these planetesimals. Therefore the mid-IR spectra in this study must also be representative of the bulk of the meteoritic material. The drilling method used to free sample material from the meteorite for measurements enabled us to sample the bulk of the meteorite. With the drill we sampled a ~ 60 mm³ volume of the meteorite. To further ensure we obtain mid-IR spectra of the bulk meteoritic material, we measured the meteorites several times, using different sample locations of the meteorite. In the final measurements no differences between different sample areas of the same meteorite were seen.

3. Results

In Fig. 1 we show the measured meteorite mid-IR spectra. From the spectra we can directly observe that those of the OC (H, L and LL types) all look very similar. In the 10-micron region (roughly from 7-13 μm) we see one large broad feature (due to amorphous silicates) and on top of this we recognise a sharp feature on the blue and the red side. In the 13-17 μm range we find four weak but distinct features. At longer wavelengths we recognise a strong feature at 19 and 24 μm .

The spectra of the HED meteorites look different from the ordinary chondrites, except for Bialystok whose spectrum closely

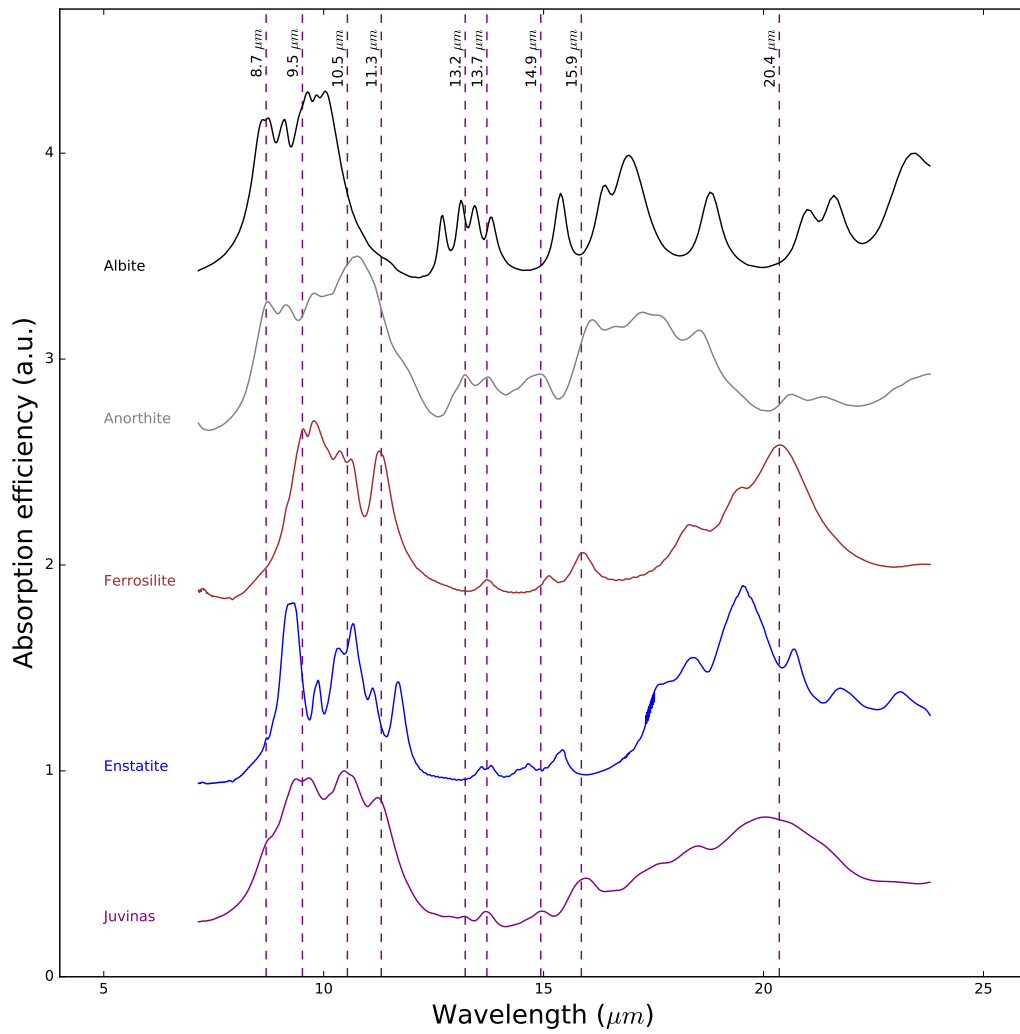


Figure 4: Comparing the Juvinas (purple) spectrum with Albite (black), Anorthite (grey), ferrosillite (brown) and enstatite (blue). Purple dashed vertical lines indicate features spotted in the Juvinas spectrum. Laboratory spectra of Anorthite (grey) and Albite (black) measured by Salisbury et al. (1991). Wavelength peak positions of bands in these spectra close to the bands of olivine and pyroxene are indicated in the plot.

resembles that of the ordinary chondrites. The other HED meteorites show a strong triple structure on top of the 10 μm complex and they only have three weak bands in the 13-17 μm region. In the 19-24 μm region the HED meteorites show a 19 μm band and Juvinas, Luotolax and Stannern also seem to have a broad feature around 26 μm , but this is very close to the end of the wavelength range that we were able to measure.

The pallasite spectrum shows two strong sharp bands in the 10 μm region and a band at 16 μm . Similar to the ordinary chondrites the pallasite also shows a 19 and 24 μm feature.

In Fig. 2 we show averaged spectra of the OC and HED group meteorites in order to study their general spectral properties. In the figure we compare the meteorite spectra to laboratory measurements of forsterite (Mg-rich olivine, Koike et al. 2003) and enstatite (Mg-rich pyroxene, Chihara et al. 2002), which allow us to identify all the spectral features. The pure Mg-rich olivine and pure Mg-rich pyroxene laboratory measurements shown in Fig. 2 are measured with the same method as the meteorite spectra presented in this work.

In Fig 1 and Fig. 2 we indicated the positions of the most notable features in the spectra of Mg-rich olivine and Mg-rich pyroxene as "forks". In the spectra of ordinary chondrites we can now identify the sharp features on the blue ($\sim 9 \mu\text{m}$) and red ($\sim 11 \mu\text{m}$) flank of the 10 μm complex as pyroxene and olivine respectively. Of the four bands in the 13-17 μm region of the ordinary chondrites the first three are from pyroxene and the one at 16 μm is from olivine. The 19 μm band in the ordinary chondrite spectra is a combination of olivine and pyroxene. The strong and broad band at $\sim 24 \mu\text{m}$ is from olivine. The features in the ordinary chondrite spectra confirm that these meteorites contain significant amounts of olivine and pyroxene. When we closely inspect the wavelength position of the features in the 13-17 μm range and of the 24 μm band, we see that the features in ordinary chondrites are red shifted compared to those of Mg-rich olivine and Mg-rich pyroxene. We know that most features of olivine and pyroxene shift to longer wavelengths as the iron content of the mineral increases (Koike et al. 2003; Chihara et al. 2002). This shift is most notable for features in the 15-30 μm range compared to the features in the 10-micron complex. Thus we can already see that the olivine and pyroxene in the ordinary chondrites contain more iron than the Mg-rich olivine and pyroxene plotted in Fig. 1 and Fig. 2.

Comparing the HED spectra to those of Mg-rich olivine and Mg-rich pyroxene we see that all (except Bialystok) HED spectra are very similar to that of pyroxene. They all have the three peaks in the 10 μm range as well as the three weak bands in the 13-17 μm region. In the HED spectra we do not recognise any olivine, since we see no bands at 16 or 24 μm . When we inspect the wavelength positions of the features in the 13-17 μm range we see that the bands in the HED spectra are red shifted compared to Mg-rich pyroxene. This indicates that the pyroxene in the HED could contain significant amounts of iron. Bialystok is an exceptional HED in our sample since its mid-IR spectra looks similar to the ordinary chondrites and thus shows features of both olivine and pyroxene.

HED meteorites (and especially eucrites) are known to contain plagioclase minerals. To investigate if plagioclase fea-

tures are visible in the measured spectra, we compare the spectrum of Juvinas to that of albite ($\text{NaAlSi}_3\text{O}_8$) and anorthite ($\text{CaAl}_2\text{Si}_2\text{O}_8$) in Fig. 4 (Salisbury et al., 1991). We also show the spectrum of the Mg and Fe rich end members of pyroxene. Fig. 4 shows that the spectrum of Juvinas is dominated by that of Fe-rich pyroxenes. At 8.7 and 13.2 μm we see distinct, although weak, bands of anorthite. At 9.5, 13.7 and 15 μm we likely have a blend of anorthite and pyroxene bands.

The last spectrum we measured is the pallasite spectrum and we can directly recognise its spectrum as olivine without any signs of pyroxene or other minerals. Comparing the pallasite spectrum to Mg-rich olivine we see that the 16 and 24 μm bands of the pallasite are red shifted and thus the olivine will contain some amounts of Fe. Interesting about the peak positions of the bands in the pallasite spectrum is that the amount by which the features are shifted is less than the shift for the ordinary chondrites. This hints at a lower iron content of the olivine in the pallasite compared to the ordinary chondrites.

Fig. 2 shows the averaged spectra of the meteorites measured in this work, but also includes the averaged spectra of carbonaceous chondrites (CC) measured by Beck et al. (2014). We have subdivided and averaged the CC meteorites into two groups: one containing the CC meteorites with metamorphic grades 1 and 2 and one group with grades of 3, 4 and 5. The type 1 and 2 CC meteorites have been aqueously altered, where 3, 4 and 5 have not and 4 and 5 have equilibrated due to heating in their parent body. The averaged spectrum of the CC type <3 meteorites is dominated by hydrosilicates, which shows broad bands at 10, 15 and 22 μm (see Beck et al. 2014). The type <3 CC meteorites show very weak but still distinguishable olivine bands at 11 μm and for some spectra at 16 μm (not recognisable in the averaged spectrum, see Beck et al. 2014). In contrast, the CC type ≥ 3 spectra are dominated by olivine and in some cases minor bands of pyroxene can be detected (for example at 9 μm).

Now that we have a full overview of the spectra of different meteorite groups in Fig. 2, it is interesting that these five groups look very different, meaning that we can spectroscopically recognise them. In the next section we will study the wavelength position of the olivine and pyroxene features in the meteorite spectra in more detail.

4. Quantifying the spectral differences between the meteorite groups

In this section we will study the spectral difference between the meteoritic groups in a quantitative way. We will get a measure of the ratio of pyroxene to olivine in the meteorites by calculating the $\frac{Py}{Py+Ol}$ ratio. For *Py* and *Ol* we take the integrated strength of the 15 μm and 16 μm bands for pyroxene and olivine respectively. In choosing these features it was important to pick two features that are close together in order to minimise any wavelength and temperature effects. For example in astronomical spectra the emission of the features is dependent on temperature in addition to abundance, but the temperature effect is divided out in the ratio when the features are close together in wavelength. Another set of features to consider for the pyroxene over olivine ratio are the 9 μm and 11 μm bands.

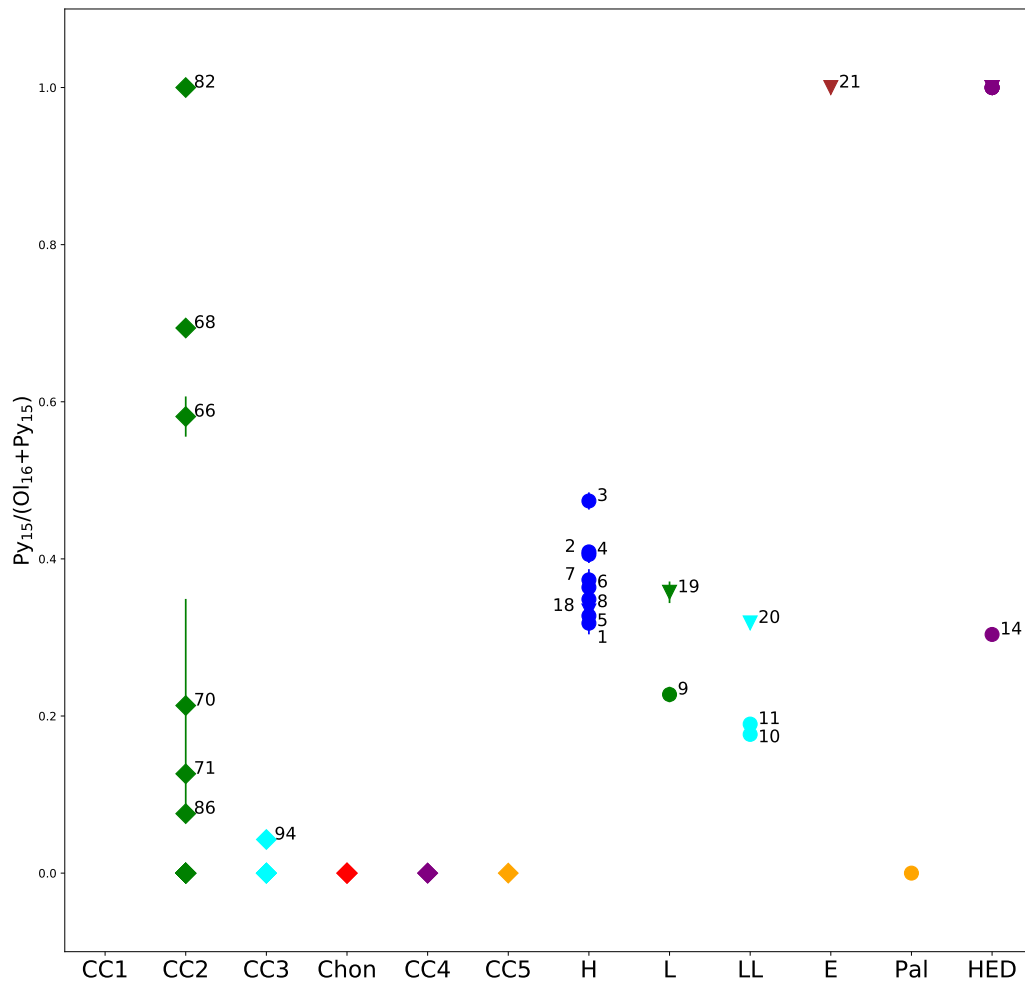


Figure 5: The $\frac{Py}{Py+Ol}$ ratio for the different meteorite groups as determined from the 15 and 16 μm bands. *CC1*, *CC2*, up to *CC5* stands for carbonaceous chondrites of metamorphic grade 1 and up. *Chon.* stands for chondrules, which are the chondrules of the Allende meteorite (#88). *H*, *L* and *LL* stand for ordinary chondrites of that type, *E* stands for enstatite chondrites and *Pal.* for pallasite. For clarity some data points are not numbered when the ratio is either one or zero, the source numbers can be deduced from the numbering of the other sources in their group. The blue, green, cyan, purple and orange dots and triangles are data points for the OC H-type, OC L-type, OC LL-type, HED and pallasite meteorites respectively. The dots are the meteorites presented in this work, while the triangles are meteorites of Morlok et al. (2012, 2014a). The blue, green, cyan, purple and orange diamonds are the type 1, 2, 3, 4, 5 CC meteorites (Beck et al., 2014) and the red diamonds are the chondrules of the Allende meteorite (Morlok et al., 2014a)

The difficulty with the 11 μm band of olivine is that it overlaps with a pyroxene band at the same wavelength. Also the strength and wavelength position of these two features are very sensitive to grain size (de Vries et al. 2015), making them a less ideal choice.

We study the shift in the olivine and pyroxene features by measuring the peak wavelength positions for two features for each mineral. For olivine we will focus on the features at 16 and 24 μm . Both these features are nicely isolated (do not overlap with pyroxene features) and can therefore be easily measured. These two features also show prominent shifts due to increasing iron content in their lattice (Koike et al., 2003). For pyroxene we will measure the feature at 9 and 15 μm for similar reasons.

4.1. Method of measuring spectral feature properties

In order to measure the wavelength peak positions and the strength of features we construct a continuum under each feature. For this we define a region to the left and right of the feature and fit a spline through the continuum points (the continua points used are listed for all objects in Tab. 6 in the appendix). The spline fit is done using *interpolate.splrep* from the *Scipy Python* package. In order to measure the peak position the continuum subtracted feature is then fitted with a spline to smooth the spectrum. The peak wavelength position is then found by finding the root of the derivative of the spline of the continuum subtracted feature (using the *Scipy* function *scipy.optimize.fsolve*). For the ratio $\frac{P_y}{P_y+O_l}$ we measure the integrated strength of the features by integrating over the continuum subtracted transmission efficiency. An example of the continua and splines we obtain are given in Fig. 3.

In order to estimate the errors in the derived peak positions and feature strengths, we use a Monte Carlo approach. We calculate these values for features at 1000 iterations and at every iteration we vary our choice of the continuum points left and right of the feature. We randomly vary the boundaries of the continua we choose left and right of the feature at every iteration by 15 % using a uniform distribution (using the *Python* standard *random.uniform*). The peak position and strength of the feature is then estimated by taking the average over all iteration. The error we state in this paper is the standard deviation of the peak position or strength of the feature over all iterations. The resulting values we measured for all spectra mentioned in this paper are listed in Tab. 3, 4 and 5.

4.2. Pyroxene over olivine ratio

In Fig. 5 we show the $\frac{P_y}{P_y+O_l}$ ratio for every meteorite group discussed in this paper. It shows that the OC consistently have a high $\frac{P_y}{P_y+O_l}$ ratio, where the H-type have the highest at 0.4 and it drops to 0.2 for the L and LL chondrites. The HED (except Bialystok #14, which is similar to the OC) and the enstatite chondrite have ratios of 1.0. All the CC have a ratio of 0.0, except for the type-2 carbonaceous chondrites, which show a large spread. The CC type 2 that show the spread are CM and CR carbonaceous chondrites. For the pallasite meteorite we measured a ratio of 0.0.

4.3. Peak positions in synthetic mineral spectra with different iron content and grain sizes

Before reporting on the feature wavelength positions of the meteoritic spectra, we first show how the peak wavelength positions of the olivine and pyroxene bands change as a function of the Fe content of the minerals and as a function of grain size. In Fig. 6 we show the wavelength peak positions of the 16 and 24 μm bands of olivine with different Fe contents. We use the data of Koike et al. (2003) because their laboratory measurements have been done in the same way as our meteorite measurements (powdered grains embedded in a KBr pellet). The black dots connected with a solid line in Fig. 6 show how both the 16 and 24 μm bands shift to longer wavelengths as the Fe content in the olivine increases.

The black dots connected with a dashed curve in Fig. 6 show peak positions for grains with sizes of 0.1 to 3.0 μm . These peak positions are calculated from the opacities (cross sections) of grains with different sizes. These opacities were calculated from the optical constants of pure forsterite (measurements done by Servoin and Piriou 1973). For the calculations of optical constants to opacities we used a Gaussian Random Field (GRF) model for the grain shape (see Min et al. 2008). This state-of-the-art model for grains approaches the best that of irregular grains. Fig. 6 shows that as a function of grain size the 16 and 24 μm bands shift to longer wavelengths. When the grains become larger than 3 μm , the mid-IR bands start to weaken so much that they cannot be measured. The peak positions of the GRF opacities do not connect to those of the Koike et al. (2003) measurement of pure forsterite. This is likely due to effects introduced by differences in the grain shape and/or measuring technique between the GRF particles and the Koike et al. (2003) measurements.

In Fig. 7 we show a similar plot as Fig. 6, but now for the pyroxene bands at 9 and 15 μm . The solid black curve shows pyroxene for different Fe contents. We use the measurements of Chihara et al. (2002), who have measured pyroxene with different Fe contents in the same way as our meteorite spectra (powdered grains embedded in KBr pellets). Fig. 7 shows how both the 9 and 15 μm bands shift to longer wavelengths when the iron content increases in the mineral. The dashed curve shows peak positions for different grain sizes of opacities calculated with GRF particles of optical constants of enstatite (Jäger et al., 1998). The dashed curve shows that the 9 μm band is sensitive to grain size, while the 15 μm band is not.

4.4. Peak positions in meteoritic spectra

The peak positions of the olivine bands in the meteorites presented in this work (see Tab. 1) are shown in Fig. 6. Most of the HED meteorites do not show any olivine bands, except for Bialystok (#14). All the ordinary chondrites show olivine bands with very similar peak positions. The peak position of the pallasite Seymchan (#17) is also shown in Fig. 6. From Fig. 6 we see that the peak positions of the olivine bands of the ordinary chondrites compares best with those of olivine with 16-40 % iron. Among the ordinary chondrites the H-type spectra have the shortest wavelength peak positions compared to the

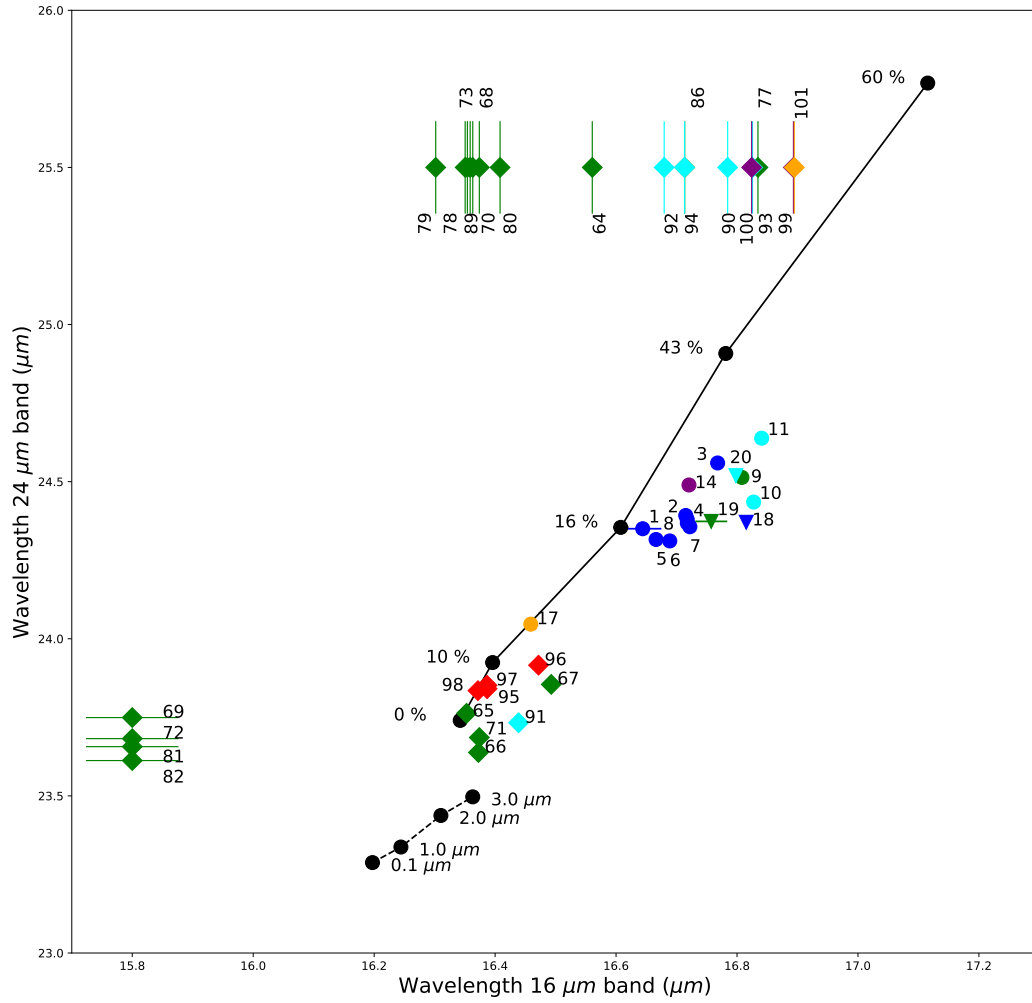


Figure 6: Wavelength peak positions of the 16 and 24 μm bands of olivine for meteorites as well as synthetic crystals. The black dots connected by a black solid line are the wavelength positions for olivine with different concentrations of Fe as measured by Koike et al. (2003). The percentage next to the dots indicates the amount of iron in the olivine. The black dots connected with a dashed line are wavelength positions for opacities of pure forsterite, calculated from optical constant measured by Servoin and Piriou (1973). The calculations from optical constants to opacities are done for different grain sizes, indicated next to the data points (further more the particle shape is according to the Gaussian Random Field method, see Min et al. (2008)). The blue, green, cyan, purple and orange dots and triangles are wavelength positions for the OC H-type, OC L-type, OC LL-type, HED and pallasite meteorites respectively. The dots are the meteorites presented in this work, while the triangles are meteorites of Morlok et al. (2012, 2014a). The blue, green, cyan, purple and orange diamonds are the type 1, 2, 3, 4, 5 CC meteorites (Beck et al., 2014) and the red diamonds are the chondrules of the Allende meteorite (Morlok et al., 2014a). Spectra for which only one of the two features could be measured the measurement is displayed as a symbol with a large bar at 15.8 μm or 25.5 μm .

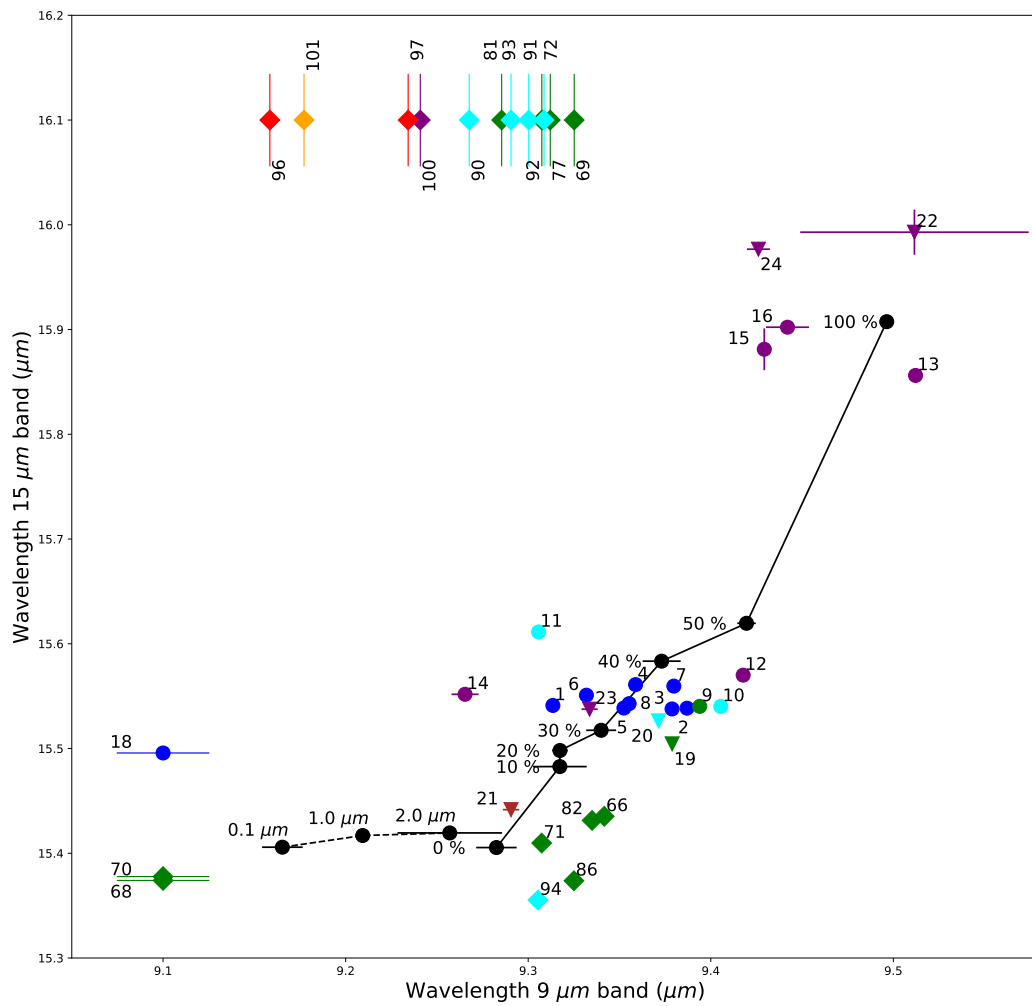


Figure 7: The same plot as Fig. 6 but for the 9 and 15 μm band of pyroxene.

L-type and LL-type, although the differences are small. The pallasite Seymchan (#17) has the bluest peak positions of its olivine bands among the meteorites presented in this work and compare best with olivine with 10-16 % iron.

The peak positions of the pyroxene bands in the meteorite sample are shown in Fig. 7. The ordinary chondrites show a spread in the peak positions of the 9 μm band, but very little variation in the 15 μm band peak position. It is difficult to say if the spread in the 9 μm band position of the OCs is due to difference in grain size or iron concentration. But we can conclude that the peak position of the OCs compares best with pyroxene that has a 10-50 % concentration of iron. In the same way we saw this for the olivine bands of Bialystok (HED, #14), the pyroxene bands of Bialystok (#14) also have peak positions very similar to those of the OCs. The pyroxene bands of the HED Shalka (#12) are also very similar to those of the OCs. The other HED meteorites have pyroxene bands very different from the OCs. Juvinas (#13), Luotolax (#15) and Stannern (#16) all have strongly red shifted 15 μm bands compared to pure enstatite. Among these three Juvinas (#13) and Stannern (#16) also have 9 μm bands that are red shifted and their peak position compares well with pyroxene with very high concentrations of iron (up to 100%, called ferrosilite). Luotolax (#15) has a 15 μm band that compares well with bands of ferrosilite, but its 9 μm band is at too short wavelengths compared to those of synthetic ferrosilite.

In Fig. 6 and 7 we also added OC and HED meteorites available from other sources. We show peak positions of the OC meteorites Cenniceros (#18), Barratta (#19) and Parnallee (#20) measured by Morlok et al. (2014a). The peak positions of these OC meteorite spectra are similar to the OC meteorites measured for this work. In Fig. 7 we also show the pyroxene peak positions of the HED meteorites measured by Morlok et al. (2012) (#22 and 24). The peak positions of these HED meteorites are closest to the bands of ferrosilite, like the HED meteorites Juvinas (#13) and Stannern (#16) from the sample presented in this work. The Morlok et al. (2012) sample also contained an enstatite chondrite, Indarch (#21). As expected this meteorite does not show olivine bands and its pyroxene bands compare best with pyroxene with low iron concentrations.

We also include the measurements of mid-IR spectra of carbonaceous chondrites. We collected carbonaceous chondrites measured by Beck et al. (2014) and mid-IR spectra of the chondrules from Allende (type CV, metamorphic grade 3, Morlok et al. 2014a). Beck et al. (2014) measured carbonaceous chondrites of metamorphic grade 1 up to 5. The mid-IR spectra of different metamorphic grades look very different (see Fig. 2). Where grade 1 is dominated by features of hydrosilicates and the spectra become increasingly more silicate-like when going to higher metamorphic grades, where type 4 and 5 can be completely dominated by olivine and some pyroxene.

Fig. 6 shows the olivine bands of the carbonaceous chondrites of Beck et al. (2014). Some of the spectra have both measurements of the 16 and 24 μm band, but most only have a 16 μm band because the measured spectra did not extend into the 24 μm range. Striking is that most type 2 and 3 carbonaceous chondrites have 16 and 24 μm bands that compare

best with laboratory measurements of 0-10% iron, while higher metamorphic grades have 16 μm bands that compare best with 15-50% iron concentrations. The chondrules of the Allende meteorite are also shown in Fig. 6 with red diamonds and they compare best with laboratory measurements with ~0-10% iron. This in contrast to the bulk measurement of Allende (#88) of Beck et al. (2014), which has a 16 μm band that compares best with 43% iron concentrations.

In Fig. 7 we show the pyroxene bands of the carbonaceous chondrites. Five meteorite spectra have both the 9 and 15 μm bands and these are of metamorphic type 2 and 3 and these bands indicate a low iron concentration for the pyroxene. There are quite a few carbonaceous chondrites that only have a 9 μm band and no 15 μm band. These 9 μm bands are weak, which might explain why the 15 μm band is not detected for these meteorites. Difficult to explain is that some of the meteorites (type 4 and 5 and Allende chondrules) have 9 μm bands that are blue shifted compared to the pure enstatite (0% iron) bands.

5. Discussion

We measured and investigated the mid-IR spectra of several groups of meteorites. In detail we studied the peak positions of the 16 and 24 μm bands of olivine, the 9 and 15 μm bands of pyroxene and the $\frac{P_y}{P_y+O_l}$ ratio. The peak positions of the spectral bands are dependent on the composition of the silicates. Through the use of the shift in the 16 and 24 μm bands of olivine we showed that the olivine iron content of ordinary chondrites ranges between 15-40 % (see Fig. 6). Here the H-type OC seem to have slightly lower olivine iron concentrations compared with the few L and LL-type OC we measured. We do not see much difference between different metamorphic grades. Similar for the 9 and 15 μm bands of pyroxene we showed that the OC have pyroxene iron concentrations between 10-50 % (see Fig. 7). Both the olivine and pyroxene compositions are consistent with detailed compositional studies which show 16-20 %, 22-26 % and 27-32 % iron concentrations in the olivine for H, L and LL-type OC respectively and 18-26 % iron concentrations in the pyroxene for H, L, LL-type meteorites (Van Schmus, 1969; Brearley and Jones, 1998). Based on the $\frac{P_y}{P_y+O_l}$ ratio we showed that the pyroxene and olivine content of OCs gives a ratio of 0.4 down to 0.2.

For many of the carbonaceous chondrites the spectra of Beck et al. (2014) did not reach long enough wavelengths to measure the 24 μm band of olivine, also many carbonaceous chondrites have such low pyroxene compositions that the 15 μm band could not be detected. The $\frac{P_y}{P_y+O_l}$ ratio showed that most carbonaceous chondrites are pyroxene poor, except for some CM and CR types that show a large spread of ratios. From the band positions in Fig. 6 we could see that the aqueously altered and un-equilibrated (metamorphic grade 2 or 3) carbonaceous chondrites have a very low (0-10 % based on the band positions) iron concentration in the olivine. This is consistent with composition measurements, which indicate olivine iron concentrations of 0-5 % for these un-equilibrated carbonaceous chondrites (Rubin et al., 1988; Kallemeyn et al., 1994;

Table 2: Meteorite parent body properties and the spectroscopic observables of their debris

Group	Parent body type	Spectrum	Peak shifts indicate Fe/(Mg+Fe)	Feature ratio $\frac{Py}{Py+Ol}$
Carbonaceous chondrites type 1 & 2	Aqueous alteration Relatively small (~10-100 km)	Hydro-silicate bands Possibly weak Ol and Py	Ol: 0.00-0.10 Py: 0.00-0.10	0.0 or a large spread
Carbonaceous chondrites type ≥ 3	Equilibration Relatively small (~10-100 km)	Olivine Weak pyroxene	Ol: 0.15-0.40	0.0
Ordinary chondrites	Equilibration Relatively small (~10-100 km)	Olivine & pyroxene	Ol: 0.15-0.40 Py: 0.10-0.50	0.2-0.4
HED	Differentiation & Igneous processes Relatively large (~250 km)	Dominated by pyroxene-like appearance	Py: High Can contain other phases then Mg-Fe-pyroxene	1.0
Pallasites	Impact-generated mixture or from crust-core boundary	Pure olivine	Ol: 0.10-0.16	0.0

Bischoff et al., 1993). From the 16 μm olivine bands for equilibrated carbonaceous chondrites (metamorphic grades 4 and 5) we find higher olivine iron concentrations, which are of the order of the concentrations in ordinary chondrites. Such higher iron concentrations in the olivine are confirmed by laboratory measurements reviewed in Hutchison (2004).

The HED meteorites in our sample consist of three groups, the eucrites, diogenites and howardites. These meteorites are rocks from a body other than Earth, the Moon or Mars, which experienced basaltic vulcanism and igneous fractionation. The most likely parent body for these meteorites is 4 Vesta (Takeda, 1997; Russell et al., 2015). HED meteorites are known to be composed mostly of pyroxene and/or plagioclase and minor amounts of other minerals (Hutchison, 2004). Here plagioclase is a solid-solution between albite ($\text{NaAlSi}_3\text{O}_8$) and anorthite ($\text{CaAl}_2\text{Si}_2\text{O}_8$). Of the HED meteorites, diogenites are rich in (>90 vol%) pyroxene, while eucrites are rich in plagioclase (>90 vol%). Diogenite's pyroxene composition ranges within $\text{Wo}_{1-4}\text{En}_{77-67}\text{Fs}_{20-29}$ (Fowler et al., 1994) (where Wo stands for wollastonite, which is a calcium-rich pyroxene end-member). The plagioclase in eucrites can have compositions of for example An_{93-80} in Juvinas (#13) and An_{89-72} in Stannern (#16) (Takeda, 1997). Howardites are surface breccias composed of diogenite, eucrite and sometimes carbonaceous chondrite debris.

The eucrites, diogenites and howardites have distinct mid-IR spectral characteristics. For example the eucrites (Juvinas #13, Stannern #16 and #22 from Morlok et al. 2012) all have pyroxene bands that compare best with Fe-rich pyroxenes. In Fig. 4 we compared the spectrum of the eucrite Juvinas to that of anorthite and albite, but we did not find strong features in the Juvinas spectrum that indicated any plagioclase. This is likely due to a difference in cross section values of pyroxene and plagioclase. The diogenites (Shalka #12 and #23 from Morlok

et al. 2012) in our sample compare well with pyroxene with iron concentrations of 20-40 %, which is similar to the range found in laboratory studies of Fs_{20-29} (Fowler et al., 1994). The pyroxene-rich nature of the HED group is reflected in the $\frac{Py}{Py+Ol}$ ratio, which is ~ 1.0 for all of them.

The howardite meteorites in our sample are all very different, which likely reflects their brecciated nature. For example some (#15 and #24) have pyroxene bands that are closest to 100% ferrosilite (like eucrites). Bialystok (#14) has pyroxene bands that compare well with diogenites. Interesting about Bialystok is that its spectrum (see Fig. 1) looks very similar to the ordinary chondrites. Bialystok is also the only HED meteorites for which we detected olivine bands. Besides the HED achondrite meteorites we also have an achondrite pallasite meteorite in our sample (Seymchan, #17). The pallasite spectrum confirms the fact that pallasites contain only the silicate olivine ($\frac{Py}{Py+Ol}$ ratio is 0.0). The pallasite's mid-IR bands compare best with olivine with an iron concentration of 10-16%.

The main result of this work is that the mid-IR spectra of debris from aqueously altered, pristine, equilibrated and differentiated parent bodies show distinct and observable differences. Or in other words, we can observe from the spectra of the debris if its parent body was wet or dry and if it was pristine, small or large. When going from an aqueously altered (small and wet) to a pristine (small), equilibrated (dry and small) and then a differentiated parent body (large), the debris of such a body will show a spectrum with a decrease in the hydrosilicate content, an increase in the pyroxene/olivine ratio and a red-shifting of the olivine bands due to an increase of iron in the olivine. These spectroscopic differences and their link to the properties of their parent bodies are summarised in Tab. 2.

Small (micron-sized) grains of olivine and pyroxene have been observed in many astronomical environments in both crystalline and amorphous form. Examples of such environments

are disks around pre-main-sequence stars (Waelkens et al., 1996; Meeus et al., 2001; Kessler-Silacci et al., 2006), main-sequence stars (Chen et al., 2007; Olofsson et al., 2012), comets (Wooden, 2002), post-main-sequence stars (Waters et al., 1996; Sylvester et al., 1999; Molster et al., 2002) and active galaxies (Markwick-Kemper et al., 2007; Spoon et al., 2006). Using the results of many studies of planet forming disks we now briefly discuss how the olivine and pyroxene in the meteorites compares with the grains found in these environments. When interpreting these studies one has to consider the techniques and laboratory measurements used to obtain the dust cross sections. The common techniques to obtain cross sections of dust grains are 1) transmission spectroscopy of in KBr embedded samples, 2) model calculations of cross-sections from optical constants (obtained from reflection measurements) and, 3) transmission spectroscopy of grains suspended in a gas (aerosol measurements). We note that the peak wavelength positions of spectral features for these measurements do not always agree (Tamanai et al., 2009). This is due, for example, the effects of the inclusion of KBr in the measured sample or due to differences in the grain shape.

The circumstellar environment where we can observe debris from planetesimals are debris disks. These are dusty disks or rings around main-sequence stars, often with planets. These disks form from proto-planetary disks when the gas and small dust grains in the disk have been lost. These disks still show emission of small dust grains, but this dust needs to be continually replenished by collisions between planetesimals (Calvet et al., 2005; Wyatt et al., 2007). Interesting about these systems is that we know that the dust comes from planetesimals and thus traces the composition of these bodies.

Olofsson et al. (2012) modelled several so called warm debris disks. These systems have dust close enough to the star for it to be at least several hundreds of Kelvin (for example Olofsson et al. (2012) derive dust temperatures of 200-1500 K at the inner-edge of the disk, depending on the dust geometry, central temperature, dust composition, and other system parameters). This makes that these objects have infrared excesses on top of the stellar spectrum starting at $\sim 5\text{-}10\ \mu\text{m}$ (Bryden et al., 2006; Chen et al., 2006). These warm debris disks are rare since most debris disks are Kuiper-belt-type disks, having no to little emission from warm dust (Liseau et al., 2010; Löhne et al., 2012). For several of the warm debris disks Olofsson et al. (2012) finds emission features of olivine (and possible pyroxene). Modelling of the mid-IR spectra Olofsson et al. (2012) report that the olivine has an iron concentration of $\sim 20\%$. For their analysis they used the aerosol measurements of Tamanai et al. (2009), which is a good comparison with the free floating grains in these disks. Olofsson et al. (2012) also found that the disks only contain minor amounts of pyroxene, where the $\text{Py}/(\text{Ol}+\text{Py})$ ratio ranged from 0 to 0.2. Thus for these warm debris disks it seems the olivine grains are rich in iron, but the pyroxene abundance is not high. Comparing these results to the meteorite groups discussed in this work, the olivine and pyroxene in these warm debris disk systems compares best to the carbonaceous chondrites type ≥ 3 or possibly pyroxene poor ordinary chondrites.

Proto-planetary disks around pre-main-sequence stars contain both dust and gas and these disks are the formation place of planets and planetesimals. In these systems the dust is probably not altered by parent-body processes, but some of the disks could be transitioning into a debris disk and in that case planetesimal debris could be present. Furthermore, the spectra of chondrites presented in this work can help us understand the dust in proto-planetary disks since these dust grains are the building blocks of ordinary chondrites (matrix, chondrules and calcium aluminum inclusions). Studies of a large set of mid-IR spectra of disks around T Tauri (Watson et al., 2009) and Herbig Ae/Be (Juhász et al., 2010; Maaskant et al., 2015) stars showed that these disks can have a variety of olivine and pyroxene abundances, ranging from only olivine to an equal mixture of the two. It is thought that the olivine, the most stable of the two, condenses from the gas in the inner parts of the disk while the pyroxene is formed in colder regions further out in the disk (Gail, 2004; Ábrahám et al., 2009; Harker and Desch, 2002). van Boekel et al. (2004) indeed showed, using interferometrical data, that for the proto-planetary disk HD 142527 the pyroxene over olivine ratio increases radially outwards. In contrast to this Juhász et al. (2010) showed, based on studying mid-IR spectra, that for a large set of proto-planetary disks the enstatite is predominantly located in the inner disk, while the olivine is located in the outer parts of the disk.

From the analysis of the mid-IR features it has been reported that the olivine is very magnesium rich in these proto-planetary disks and more recent studies including far-IR spectra concluded that the iron content of the olivine was less than 2% (Sturm et al., 2013; Maaskant et al., 2015). These studies have been done using cross sections obtained from optical constants using model calculations. These cross section calculations simulate grains in a vacuum, but since the models require one to assume a certain shape, they might not be as good a comparison to astronomical dust as the aerosol measurements used in the study of Olofsson et al. (2012). Besides the mid-IR astronomical spectra these studies also used the Herschel far-IR spectra with an olivine resonance at $69\ \mu\text{m}$ band. The low iron concentration of the olivine and the presence of significant amounts of pyroxene makes that the dust in these proto-planetary disks resembles the carbonaceous chondrites of type-2, but one has to keep in mind that the dust in these disks likely does not come from collisions, but from gas phase condensation and/or annealing.

6. Conclusions

In this work we showed that, and how, the different groups of meteorites can be distinguished when they would be spectroscopically studied in the form of debris. Since the different groups of meteorites can be traced back to parent bodies with different properties we can spectroscopically probe planetesimal properties (like size and its thermal and igneous evolution). The minerals of different meteorite groups can be spectroscopically distinguished by 1) the pyroxene-olivine ratio and 2) the iron in the olivine. These two properties can be measured in the

mid-IR spectra by measuring feature strength ratios and peak shifts.

References

- Ábrahám, P., Juhász, A., Dullemond, C. P., Kóspál, Á., van Boekel, R., Bouwman, J., Henning, T., Moór, A., Mosoni, L., Sicilia-Aguilar, A., Sipos, N., May 2009. Episodic formation of cometary material in the outburst of a young Sun-like star. *Nature*459, 224–226.
- Beck, P., Garenne, A., Quirico, E., Bonal, L., Montes-Hernandez, G., Moynier, F., Schmitt, B., Feb. 2014. Transmission infrared spectra (2–25 μm) of carbonaceous chondrites (CI, CM, CV-CK, CR, C2 ungrouped): Mineralogy, water, and asteroidal processes. *Icarus*229, 263–277.
- Bischoff, A., Palme, H., Schultz, L., Weber, D., Weber, H. W., Spettel, B., Jun. 1993. ACFER 182 and paired samples, an iron-rich carbonaceous chondrite - Similarities with ALH85085 and relationship to CR chondrites. *Geochim. Cosmochim. Acta*57, 2631–2648.
- Bowey, J. E., Morlok, A., Köhler, M., Grady, M., Apr. 2007. 2–16 μm spectroscopy of micron-sized enstatite (Mg,Fe)₂Si₂O₆ silicates from primitive chondritic meteorites. *MNRAS*376, 1367–1374.
- Bradley, J. P., Keller, L. P., Snow, T. P., Hanner, M. S., Flynn, G. J., Gezo, J. C., Clemett, S. J., Brownlee, D. E., Bowey, J. E., Sep. 1999. An infrared spectral match between GEMS and interstellar grains. *Science* 285.
- Brearley, A., Jones, R., 1998. Chondritic meteorites. *Planetary Materials* 398, 3–13.
- Bryden, G., Beichman, C. A., Trilling, D. E., Rieke, G. H., Holmes, E. K., Lawler, S. M., Stapelfeldt, K. R., Werner, M. W., Gautier, T. N., Blaylock, M., Gordon, K. D., Stansberry, J. A., Su, K. Y. L., Jan. 2006. Frequency of Debris Disks around Solar-Type Stars: First Results from a Spitzer MIPS Survey. *ApJ*636, 1098–1113.
- Calvet, N., D'Alessio, P., Watson, D. M., Franco-Hernández, R., Furlan, E., Green, J., Sutter, P. M., Forrest, W. J., Hartmann, L., Uchida, K. I., Keller, L. D., Sargent, B., Najita, J., Herter, T. L., Barry, D. J., Hall, P., Sep. 2005. Disks in Transition in the Taurus Population: Spitzer IRS Spectra of GM Aurigae and DM Tauri. *ApJ*630, L185–L188.
- Chen, C. H., Li, A., Bohac, C., Kim, K. H., Watson, D. M., van Cleve, J., Houck, J., Stapelfeldt, K., Werner, M. W., Rieke, G., Su, K., Marengo, M., Backman, D., Beichman, C., Fazio, G., Sep. 2007. The Dust and Gas Around β Pictoris. *ApJ*666, 466–474.
- Chen, C. H., Sargent, B. A., Bohac, C., Kim, K. H., Leibensperger, E., Jura, M., Najita, J., Forrest, W. J., Watson, D. M., Sloan, G. C., Keller, L. D., Sep. 2006. Spitzer IRS Spectroscopy of IRAS-discovered Debris Disks. *ApJS*166, 351–377.
- Chihara, H., Koike, C., Tsuchiyama, A., Tachibana, S., Sakamoto, D., Aug. 2002. Compositional dependence of infrared absorption spectra of crystalline silicates. I. Mg-Fe pyroxenes. *A&A*391, 267–273.
- Consolmagno, G. J., Drake, M. J., Sep. 1977. Composition and evolution of the eucrite parent body - Evidence from rare earth elements. *Geochim. Cosmochim. Acta*41, 1271–1282.
- de Vries, B. L., Acke, B., Blommaert, J. A. D. L., Waelkens, C., Waters, L. B. F. M., Vandenbussche, B., Min, M., Olofsson, G., Dominik, C., Decin, L., Barlow, M. J., Brandeker, A., di Francesco, J., Glauser, A. M., Greaves, J., Harvey, P. M., Holland, W. S., Ivison, R. J., Liseau, R., Pantin, E. E., Pilbratt, G. L., Royer, P., Sibthorpe, B., Oct. 2012. Comet-like mineralogy of olivine crystals in an extrasolar proto-Kuiper belt. *Nature*490, 74–76.
- de Vries, B. L., Maaskant, K. M., Min, M., Lombaert, R., Waters, L. B. F. M., Blommaert, J. A. D. L., Apr. 2015. Micron-sized forsterite grains in the pre-planetary nebula of IRAS 17150-3224. Searching for clues to the mysterious evolution of massive AGB stars. *A&A*576, A98.
- Fowler, G. W., Papike, J. J., Spilde, M. N., Shearer, C. K., Sep. 1994. Diogenites as asteroidal cumulates: Insights from orthopyroxene major and minor element chemistry. *Geochim. Cosmochim. Acta*58, 3921–3929.
- Gail, H.-P., Jan. 2004. Radial mixing in protoplanetary accretion disks. IV. Metamorphosis of the silicate dust complex. *A&A*413, 571–591.
- Gail, H.-P., Sedlmayr, E., Jul. 1999. Mineral formation in stellar winds. I. Condensation sequence of silicate and iron grains in stationary oxygen rich outflows. *A&A*347, 594–616.
- Harker, D. E., Desch, S. J., Feb. 2002. Annealing of Silicate Dust by Nebular Shocks at 10 AU. *ApJ*565, L109–L112.
- Hutchison, R., Oct. 2004. *Meteorites*. Cambridge University Press.
- Jäger, C., Molster, F. J., Dorschner, J., Henning, T., Mutschke, H., Waters, L. B. F. M., Nov. 1998. Steps toward interstellar silicate mineralogy. IV. The crystalline revolution. *A&A*339, 904–916.
- Juhász, A., Bouwman, J., Henning, T., Acke, B., van den Ancker, M. E., Meeus, G., Dominik, C., Min, M., Tielens, A. G. G. M., Waters, L. B. F. M., Sep. 2010. Dust Evolution in Protoplanetary Disks Around Herbig Ae/Be Stars - the Spitzer View. *ApJ*721, 431–455.
- Kallemeyn, G. W., Rubin, A. E., Wasson, J. T., Jul. 1994. The compositional classification of chondrites: VI. The CR carbonaceous chondrite group. *Geochim. Cosmochim. Acta*58, 2873–2888.
- Kemper, F., Vriend, W. J., Tielens, A. G. G. M., Jul. 2004. The Absence of Crystalline Silicates in the Diffuse Interstellar Medium. *ApJ*609, 826–837.
- Kessel, R., Beckett, J. R., Stolper, E. M., Apr. 2007. The thermal history of equilibrated ordinary chondrites and the relationship between textural maturity and temperature. *Geochim. Cosmochim. Acta*71, 1855–1881.
- Kessler-Silacci, J., Augereau, J.-C., Dullemond, C. P., Geers, V., Lahuis, F., Evans, II, N. J., van Dishoeck, E. F., Blake, G. A. and Boogert, A. C. A., Brown, J., Jørgensen, J. K., Knez, C., Pontoppidan, K. M., Mar. 2006. c2d Spitzer IRS Spectra of Disks around T Tauri Stars. I. Silicate Emission and Grain Growth. *ApJ*639, 275–291.
- Koike, C., Chihara, H., Tsuchiyama, A., Suto, H., Sogawa, H., Okuda, H., Mar. 2003. Compositional dependence of infrared absorption spectra of crystalline silicate. II. Natural and synthetic olivines. *A&A*399, 1101–1107.
- Liseau, R., Eiroa, C., Fedele, D., Augereau, J.-C., Olofsson, G., González, B., Maldonado, J., Montesinos, B., Mora, A., Absil, O., Ardila, D., Barrado, D., Bayo, A., Beichman, C. A., Bryden, G., Danchi, W. C., Del Burgo, C., Ertel, S., Fridlund, C. W. M., Heras, A. M., Krivov, A. V., Launhardt, R., Lebreton, J., Löhne, T., Marshall, J. P., Meeus, G., Müller, S., Pilbratt, G. L., Roberge, A., Rodmann, J., Solano, E., Stapelfeldt, K. R., Thébault, P., White, G. J., Wolf, S., Jul. 2010. Resolving the cold debris disc around a planet-hosting star. PACS photometric imaging observations of η Eridani (HD 10647, HR 506). *A&A*518, L132.
- Löhne, T., Augereau, J.-C., Ertel, S., Marshall, J. P., Eiroa, C., Mora, A., Absil, O., Stapelfeldt, K., Thébault, P., Bayo, A., Del Burgo, C., Danchi, W., Krivov, A. V., Lebreton, J., Letawe, G., Magain, P., Maldonado, J., Montesinos, B., Pilbratt, G. L., White, G. J., Wolf, S., Jan. 2012. Modelling the huge, Herschel-resolved debris ring around HD 207129. *A&A*537, A110.
- Maaskant, K. M., de Vries, B. L., Min, M., Waters, L. B. F. M., Dominik, C., Molster, F., Tielens, A. G. G. M., Feb. 2015. Location and sizes of forsterite grains in protoplanetary disks. Interpretation from the Herschel DIGIT programme. *A&A*574, A140.
- Markwick-Kemper, F., Gallagher, S. C., Hines, D. C., Bouwman, J., Oct. 2007. Dust in the Wind: Crystalline Silicates, Corundum, and Periclase in PG 2112+059. *ApJ*668, L107–L110.
- McCord, T. B., Adams, J. B., Johnson, T. V., Jun. 1970. Asteroid Vesta: Spectral Reflectivity and Compositional Implications. *Science* 168, 1445–1447.
- Meeus, G., Waters, L. B. F. M., Bouwman, J., van den Ancker, M. E., Waelkens, C., Malfait, K., Jan. 2001. ISO spectroscopy of circumstellar dust in 14 Herbig Ae/Be systems: Towards an understanding of dust processing. *A&A*365, 476–490.
- Min, M., Hovenier, J. W., Waters, L. B. F. M., de Koter, A., Oct. 2008. The infrared emission spectra of compositionally inhomogeneous aggregates composed of irregularly shaped constituents. *A&A*489, 135–141.
- Min, M., Waters, L. B. F. M., de Koter, A., Hovenier, J. W., Keller, L. P., Markwick-Kemper, F., Feb. 2007. The shape and composition of interstellar silicate grains. *A&A*462, 667–676.
- Molster, F. J., Demyk, A., D'Hendecourt, L., Bradley, J. P., Mar. 2003. The First 2–50 μm Infrared Spectrum of an Interplanetary Dust Particle (IDP). In: Mackwell, S., Stansberry, E. (Eds.), *Lunar and Planetary Science Conference*. Vol. 34 of Lunar and Planetary Inst. Technical Report. p. 1148.
- Molster, F. J., Waters, L. B. F. M., Tielens, A. G. G. M., Barlow, M. J., Jan. 2002. Crystalline silicate dust around evolved stars. I. The sample stars. *A&A*382, 184–221.
- Morlok, A., Koike, C., Tomeoka, K., Mason, A., Lisse, C., Anand, M., Grady, M., May 2012. Mid-infrared spectra of differentiated meteorites (achondrites): Comparison with astronomical observations of dust in protoplanetary and debris disks. *Icarus*219, 48–56.
- Morlok, A., Koike, C., Tomioka, N., Mann, I., Tomeoka, K., May 2010. Mid-infrared spectra of the shocked Murchison CM chondrite: Comparison with astronomical observations of dust in debris disks. *Icarus*207, 45–53.
- Morlok, A., Lisse, C. M., Mason, A. B., Bullock, E. S., Grady, M. M., Mar.

- 2014a. Mid-infrared spectroscopy of components in chondrites: Search for processed materials in young Solar Systems and comets. *Icarus* 231, 338–355.
- Morlok, A., Mason, A. B., Anand, M., Lisse, C. M., Bullock, E. S., Grady, M. M., Sep. 2014b. Dust from collisions: A way to probe the composition of exo-planets? *Icarus* 239, 1–14.
- Nakamura, T., Noguchi, T., Tanaka, M., Zolensky, M. E., Kimura, M., Tsuchiyama, A., Nakato, A., Ogami, T., Ishida, H., Uesugi, M., Yada, T., Shirai, K., Fujimura, A., Okazaki, R., Sandford, S. A., Ishibashi, Y., Abe, M., Okada, T., Ueno, M., Mukai, T., Yoshikawa, M., Kawaguchi, J., Aug. 2011. Itokawa Dust Particles: A Direct Link Between S-Type Asteroids and Ordinary Chondrites. *Science* 333, 1113–.
- Olofsson, J., Juhász, A., Henning, T., Mutschke, H., Tamanai, A., Moór, A., Ábrahám, P., Jun. 2012. Transient dust in warm debris disks. Detection of Fe-rich olivine grains. *A&A* 542, A90.
- Ordal, M. A., Bell, R. J., Alexander, Jr., R. W., Newquist, L. A., Querry, M. R., Mar. 1988. Optical properties of Al, Fe, Ti, Ta, W, and Mo at submillimeter wavelengths. *Appl. Opt.* 27, 1203–1209.
- Rubin, A. E., Wang, D., Kallemeyn, G. W., Wasson, J. T., Mar. 1988. The Ningqiang meteorite - Classification and petrology of an anomalous CV chondrite. *Meteoritics* 23, 13–23.
- Russell, C. T., McSween, H. Y., Jaumann, R., Raymond, C. A., 2015. The Dawn Mission to Vesta and Ceres. pp. 419–432.
- Salisbury, J. W., Walter, L. S., Vergo, N., D’Aria, D., 1991. *Infrared (2.1-25 micron) Spectra of Minerals*. Johns Hopkins University Press.
- Sandford, S. A., Walker, R. M., Apr. 1985. Laboratory infrared transmission spectra of individual interplanetary dust particles from 2.5 to 25 microns. *ApJ* 291, 838–851.
- Sargent, B. A., Forrest, W. J., Tayrien, C., McClure, M. K., Watson, D. M., Sloan, G. C., Li, A., Manoj, P., Bohac, C. J., Furlan, E., Kim, K. H., Green, J. D., Jun. 2009. Dust Processing and Grain Growth in Protoplanetary Disks in the Taurus-Auriga Star-Forming Region. *ApJS* 182, 477–508.
- Servoin, J. L., Piriou, B., 1973. Infrared reflectivity and Raman scattering of Mg₂SiO₄ single crystal. *Phys. Status Solidi (B)* 55, 677–686.
- Sogawa, H., Kozasa, T., May 1999. On the Origin of Crystalline Silicate in Circumstellar Envelopes of Oxygen-rich Asymptotic Giant Branch Stars. *ApJ* 516, L33–L36.
- Spoon, H. W. W., Tielens, A. G. G. M., Armus, L., Sloan, G. C., Sargent, B., Cami, J., Charmandaris, V., Houck, J. R., Soifer, B. T., Feb. 2006. The Detection of Crystalline Silicates in Ultraluminous Infrared Galaxies. *ApJ* 638, 759–765.
- Sturm, B., Bouwman, J., Henning, T., Evans, N. J., Waters, L. B. F. M., van Dishoeck, E. F., Green, J. D., Olofsson, J., Meeus, G., Maaskant, K., Dominik, C., Augereau, J. C., Mulders, G. D., Acke, B., Merin, B., Herczeg, G. J., May 2013. The 69 μ m forsterite band in spectra of protoplanetary disks. Results from the Herschel DIGIT programme. *A&A* 553, A5.
- Sylvester, R. J., Kemper, F., Barlow, M. J., de Jong, T., Waters, L. B. F. M., Tielens, A. G. G. M., Omont, A., Dec. 1999. 2.4-197 μ m spectroscopy of OH/IR stars: the IR characteristics of circumstellar dust in O-rich environments. *A&A* 352, 587–599.
- Takeda, H., Nov. 1997. Mineralogical records of early planetary processes on the HED parent body with reference to Vesta. *Meteoritics and Planetary Science* 32.
- Tamanai, A., Mutschke, H., Blum, J., Dec. 2009. IR Spectroscopic Measurements of Free-Flying Silicate Dust Grains. In: Henning, T., Grün, E., Steinacker, J. (Eds.), *Cosmic Dust - Near and Far*. Vol. 414 of *Astronomical Society of the Pacific Conference Series*. p. 438.
- Tielens, A. G. G. M., Waters, L. B. F. M., Molster, F. J., Justtanont, K., 1998. Circumstellar Silicate Mineralogy. *Ap&SS* 255, 415–426.
- van Boekel, R., Min, M., Leinert, C., Waters, L. B. F. M., Richichi, A., Chesneau, O., Dominik, C., Jaffe, W., Dutrey, A., Graser, U., Henning, T., de Jong, J., Köhler, R., de Koter, A., Lopez, B., Malbet, F., Morel, S., Paresce, F., Perrin, G., Preibisch, T., Przygodda, F., Schöller, M., Wittkowski, M., Nov. 2004. The building blocks of planets within the ‘terrestrial’ region of protoplanetary disks. *Nature* 432, 479–482.
- Van Schmus, W., 1969. Mineralogy, petrology and classification of types 3 and 4 carbonaceous chondrites. *Meteorite Research* 480, 480–91.
- Waelkens, C., Waters, L. B. F. M., de Graauw, M. S., Huygen, E., Malfait, K., Plets, H., Vandenbussche, B., Beintema, D. A. and Boxhoorn, D. R., Habing, H. J., Heras, A. M., Kester, D. J. M., Lahuis, F., Morris, P. W., Roelfsema, P. R., Salama, A., Siebenmorgen, R., Trams, N. R., van der Blik, N. R., Valentijn, E. A., Wesselius, P. R., Nov. 1996. SWS observations of young main-sequence stars with dusty circumstellar disks. *A&A* 315, L245–L248.
- Waters, L. B. F. M., Molster, F. J., de Jong, T., Beintema, D. A., Waelkens, C., Boogert, A. C. A., Boxhoorn, D. R., de Graauw, T. and Drapatz, S., Feuchtgruber, H., Genzel, R., Helmich, F. P., Heras, A. M., Huygen, R., Izumiura, H., Justtanont, K., Kester, D. J. M. and Kunze, D., Lahuis, F., Lamers, H. J. G. L. M., Leech, K. J., Loup, C., Lutz, D., Morris, P. W., Price, S. D., Roelfsema, P. R., Salama, A., Schaeidt, S. G., Tielens, A. G. G. M., Trams, N. R., Valentijn, E. A., Vandenbussche, B., van den Ancker, M. E., van Dishoeck, E. F., Van Winckel, H., Wesselius, P. R., Young, E. T., Nov. 1996. Mineralogy of oxygen-rich dust shells. *A&A* 315, L361–L364.
- Watson, D. M., Leisenring, J. M., Furlan, E., Bohac, C. J., Sargent, B., Forrest, W. J., Calvet, N., Hartmann, L., Nordhaus, J. T., Green, J. D., Kim, K. H., Sloan, G. C., Chen, C. H., Keller, L. D., d’Alessio, P., Najita, J., Uchida, K. I., Houck, J. R., Jan. 2009. Crystalline Silicates and Dust Processing in the Protoplanetary Disks of the Taurus Young Cluster. *ApJS* 180, 84–101.
- Wooden, D. H., Oct. 2002. Comet Grains: Their IR Emission and Their Relation to ISM Grains. *Earth Moon and Planets* 89, 247–287.
- Wyatt, M. C., Sep. 2008. Evolution of Debris Disks. *ARA&A* 46, 339–383.
- Wyatt, M. C., Smith, R., Su, K. Y. L., Rieke, G. H., Greaves, J. S., Beichman, C. A., Bryden, G., Jul. 2007. Steady State Evolution of Debris Disks around A Stars. *ApJ* 663, 365–382.
- Zolensky, M., Nakamura-Messenger, K., Rietmeijer, F., Leroux, H., Mikouchi, T., Ohsumi, K., Simon, S., Grossman, L., Stephan, T., Weisberg, M., Velbel, M., Zega, T., Stroud, R., Tomeoka, K., Ohnishi, I., Tomioka, N., Nakamura, T., Matrajt, G., Joswiak, D., Brownlee, D., Langenhorst, F., Krot, A., Kearsley, A., Ishii, H., Graham, G., Dai, Z. R., Chi, M., Bradley, J., Hagiya, K., Gounelle, M., Bridges, J., Feb. 2008. Comparing Wild 2 particles to chondrites and IDPs. *Meteoritics and Planetary Science* 43, 261–272.

Appendix

Table 3: Spectral feature fitting information part 1

#	Name	Type	16 μm band	24 μm band	9 μm band	15 μm band	Py/(Ol+Py)	Ref.
1	Charsonville	H 6	16.64+/-0.031	24.35+/-0.001	9.31+/-0.002	15.54+/-0.0	0.32+/-0.01	-
2	Hessle	H 5	16.72+/-0.004	24.39+/-0.001	9.39+/-0.001	15.54+/-0.001	0.41+/-0.01	-
3	Bremervorde	H 3	16.77+/-0.004	24.56+/-0.016	9.38+/-0.001	15.54+/-0.001	0.47+/-0.01	-
4	Pultusk	H 5	16.72+/-0.001	24.38+/-0.001	9.36+/-0.001	15.56+/-0.001	0.41+/-0.01	-
5	Menow	H 4	16.67+/-0.004	24.32+/-0.002	9.35+/-0.001	15.54+/-0.0	0.33+/-0.0	-
6	Stalldalen	H 5	16.69+/-0.001	24.31+/-0.001	9.33+/-0.001	15.55+/-0.001	0.36+/-0.01	-
7	Bjelaja	H 6	16.72+/-0.002	24.36+/-0.001	9.38+/-0.001	15.56+/-0.001	0.37+/-0.01	-
8	Ochansk	H 4	16.72+/-0.003	24.37+/-0.001	9.36+/-0.001	15.54+/-0.002	0.35+/-0.02	-
9	Bjurbole	L 4	16.81+/-0.002	24.51+/-0.009	9.39+/-0.002	15.54+/-0.001	0.23+/-0.01	-
10	Soka-Banja	LL 4	16.83+/-0.0	24.44+/-0.003	9.41+/-0.002	15.54+/-0.0	0.18+/-0.0	-
11	Ensisheim	LL 6	16.84+/-0.001	24.64+/-0.0	9.31+/-0.002	15.61+/-0.001	0.19+/-0.0	-
12	Shalka	Dio	-	-	9.42+/-0.002	15.57+/-0.0	1.0+/-0.0	-
13	Juvinas	Euc	-	-	9.51+/-0.002	15.86+/-0.003	1.0+/-0.0	-
14	Bialystok	How	16.72+/-0.005	24.49+/-0.001	9.27+/-0.007	15.55+/-0.0	0.3+/-0.0	-
15	Luotolax	How	-	-	9.43+/-0.001	15.88+/-0.02	1.0+/-0.0	-
16	Stannern	Euc	-	26.03+/-0.12	9.44+/-0.012	15.9+/-0.001	1.0+/-0.0	-
17	Seymehan	Pal	16.46+/-0.001	24.05+/-0.001	-	-	0.0+/-0.0	-
18	Cennicerros	H 3.8	16.82+/-0.001	24.37+/-0.001	-	15.5+/-0.001	0.33+/-0.01	1
19	Barratta	L 3.8	16.76+/-0.027	24.37+/-0.0	9.38+/-0.001	15.5+/-0.001	0.36+/-0.01	1
20	Parnallee	LL 3.6	16.8+/-0.001	24.52+/-0.0	9.37+/-0.0	15.53+/-0.001	0.32+/-0.0	1
21	Indarch	E 4	-	-	9.29+/-0.004	15.44+/-0.001	1.0+/-0.0	1
22	Ave. Euclite	Euc	-	-	9.51+/-0.063	15.99+/-0.022	1.0+/-0.0	2
23	Ave. Diognite	Dio	-	-	9.33+/-0.004	15.54+/-0.001	1.0+/-0.0	2
24	Ave. Howardite	How	-	-	9.43+/-0.006	15.98+/-0.005	1.0+/-0.0	2

Reference numbers indicate: "-": this work, 1: Morlok et al. (2014a), 2: Morlok et al. (2012), 3: Chihara et al. (2002), 4: Koike et al. (2003), 5: Beck et al. (2014), 6: Servoin and Piriou (1973), 7: Jäger et al. (1998), 8: Salisbury et al. (1991)

Table 4: Spectral feature fitting information part 2

#	Name	Type	16 μm band	24 μm band	9 μm band	15 μm band	Py/(Ol+Py)	Ref.
31	CEn100	0	-	-	9.28 \pm 0.011	15.41 \pm 0.005	-	3
32	CEn90	10	-	-	9.32 \pm 0.015	15.48 \pm 0.002	-	3
33	CEn80	20	-	-	9.32 \pm 0.004	15.5 \pm 0.002	-	3
34	CEn70	30	-	-	9.34 \pm 0.008	15.52 \pm 0.005	-	3
35	CEn60	40	-	-	9.37 \pm 0.01	15.58 \pm 0.001	-	3
36	CEn50	50	-	-	9.42 \pm 0.005	15.62 \pm 0.001	-	3
37	CEn0	100	-	-	9.5 \pm 0.001	15.91 \pm 0.005	-	3
38	Fo100	0	16.34 \pm 0.001	23.74 \pm 0.011	-	-	-	4
39	Fo90	10	16.4 \pm 0.001	23.92 \pm 0.003	-	-	-	4
40	Fo84	16	16.61 \pm 0.013	24.35 \pm 0.001	-	-	-	4
41	Fo57	43	16.78 \pm 0.003	24.91 \pm 0.009	-	-	-	4
42	Fo40	60	17.12 \pm 0.002	25.77 \pm 0.011	-	-	-	4
43	Fo22	78	17.45 \pm 0.034	-	-	-	-	4
44	Fo16	84	17.52 \pm 0.002	-	-	-	-	4
45	Fo0	100	17.68 \pm 0.003	-	-	-	-	4
46	Fo GRF	0.1	16.2 \pm 0.001	23.29 \pm 0.0	-	-	-	6
47	Fo GRF	1.0	16.24 \pm 0.001	23.34 \pm 0.004	-	-	-	6
48	Fo GRF	2.0	16.31 \pm 0.003	23.44 \pm 0.002	-	-	-	6
49	Fo GRF	3.0	16.36 \pm 0.006	23.5 \pm 0.004	-	-	-	6
50	Fo GRF	4.0	16.33 \pm 0.008	23.41 \pm 0.011	-	-	-	6
51	Fo GRF	5.0	16.33 \pm 0.006	23.47 \pm 0.005	-	-	-	6
52	En GRF	0.1	-	-	9.17 \pm 0.011	15.41 \pm 0.005	-	7
53	En GRF	1.0	-	-	9.21 \pm 0.001	15.42 \pm 0.001	-	7
54	En GRF	2.0	-	-	9.26 \pm 0.029	15.42 \pm 0.007	-	7
55	En GRF	3.0	-	-	9.19 \pm 0.0	15.42 \pm 0.009	-	7

Table 5: Spectral feature fitting information part 3

#	Name	Type	16 μm band	24 μm band	9 μm band	15 μm band	Py/(Ol+Py)	Ref.
56	Albite	-	-	-	-	-	-	8
57	Anorthite	-	-	-	-	-	-	8
58	ORGEUIL	CI 1	-	-	-	-	-	5
59	ALH83100	CM 1	-	-	-	-	-	5
60	MET01070	CM 1	-	-	-	-	-	5
61	GRO95577	CR 1	-	-	-	-	-	5
62	MURCHISON	CM 2	-	-	-	-	-	5
63	QUE99355	CM 2	-	-	-	-	-	5
64	DOM03183	CM 2	16.56+/-0.002	-	-	-	0.0+/-0.0	5
65	WIS91600	CM 2	16.35+/-0.001	23.76+/-0.002	-	-	0.0+/-0.0	5
66	LAP02342	CR 2	16.37+/-0.002	23.64+/-0.002	9.34+/-0.001	15.44+/-0.002	0.58+/-0.03	5
67	MIL07700	CM 2	16.49+/-0.001	23.85+/-0.001	-	-	0.0+/-0.0	5
68	MCY05230	CM 2	16.37+/-0.001	-	-	15.38+/-0.001	0.69+/-0.01	5
69	EET83355	C2 2	-	23.75+/-0.006	9.33+/-0.001	-	-	5
70	QUE97990	CM 2	16.36+/-0.002	-	-	15.37+/-0.051	0.21+/-0.14	5
71	PCA91082	CR 2	16.37+/-0.0	23.69+/-0.001	9.31+/-0.001	15.41+/-0.002	0.13+/-0.01	5
72	GRA06100	CR 2	-	23.68+/-0.011	9.31+/-0.001	-	-	5
73	LON94101	CM 2	16.35+/-0.001	-	-	-	0.0+/-0.0	5
74	DOM03813	CM 2	-	-	-	-	-	5
75	EET96029	CM 2	-	-	-	-	-	5
76	DOM08003	CM 2	-	-	-	-	-	5
77	PCA02010	CM 2	16.83+/-0.001	-	9.31+/-0.0	-	0.0+/-0.0	5
78	ESSEBI	CM 2	16.35+/-0.0	-	-	-	0.0+/-0.0	5
79	TAGISHLAKE	C2 2	16.3+/-0.0	-	-	-	0.0+/-0.0	5
80	BORISKINO	CM 2	16.41+/-0.001	-	-	-	0.0+/-0.0	5
81	PCA91008	CM 2	-	23.66+/-0.003	9.29+/-0.001	-	-	5
82	GRO03116	CR 2	-	23.61+/-0.008	9.33+/-0.001	15.43+/-0.001	1.0+/-0.0	5
83	ALH84044	CM 2	-	-	-	-	-	5
84	LEW85311	CM 2	-	-	-	-	-	5
85	NOGOYA	CM 2	-	-	-	-	-	5
86	RBT04133	CR 2	16.71+/-0.001	-	9.33+/-0.001	15.37+/-0.001	0.08+/-0.0	5
87	LEW87022	CM 2	-	-	-	-	-	5
88	NIGER	CM 2	-	-	-	-	-	5
89	BELLS	CM 2	16.36+/-0.001	-	-	-	0.0+/-0.0	5
90	ALLENDE	CV 3	16.78+/-0.002	-	9.27+/-0.022	-	0.0+/-0.0	5
91	KABA	CV 3	16.44+/-0.0	23.73+/-0.002	9.3+/-0.0	-	0.0+/-0.0	5
92	GROSNAJA	CV 3	16.68+/-0.002	-	9.31+/-0.002	-	0.0+/-0.0	5
93	MOKOIA	CV 3	16.83+/-0.001	-	9.29+/-0.002	-	0.0+/-0.0	5
94	VIGARANO	CV 3	16.71+/-0.011	-	9.31+/-0.001	15.36+/-0.002	0.04+/-0.0	5
95	allende PO4	chon.	16.39+/-0.0	23.84+/-0.0	-	-	0.0+/-0.0	1
96	allende PO1	chon.	16.47+/-0.001	23.92+/-0.001	9.16+/-0.0	-	0.0+/-0.0	1
97	allende POP3	chon.	16.39+/-0.001	23.85+/-0.0	9.23+/-0.0	-	0.0+/-0.0	1
98	allende PO2	chon.	16.37+/-0.0	23.83+/-0.0	-	-	0.0+/-0.0	1

Table 6: Spectral feature continua points. Part 1

#	16 μm band	24 μm band	9 μm band	15 μm band
1	15.9, 15.99, 17.2, 17.35	21.5, 22.32, 26.61, 27.34	8.65, 8.97, 9.67, 9.87	14.99, 15.11, 15.94, 16.02
2	15.9, 16.06, 17.3, 17.51	21.44, 22.55, 26.37, 28.21	8.55, 9.01, 9.65, 9.93	14.95, 15.06, 15.96, 16.11
3	15.93, 16.16, 17.26, 17.67	21.57, 22.68, 26.29, 26.93	8.46, 8.95, 9.66, 9.83	14.94, 15.09, 16.02, 16.22
4	15.94, 16.14, 17.3, 17.6	21.4, 22.44, 26.46, 27.62	8.65, 8.94, 9.69, 9.9	14.97, 15.12, 15.99, 16.21
5	15.9, 16.05, 17.28, 17.57	21.11, 22.27, 26.56, 27.42	8.65, 9.0, 9.66, 9.95	14.93, 15.09, 15.89, 16.08
6	15.93, 16.06, 17.32, 17.72	21.23, 22.4, 26.19, 27.5	8.56, 8.93, 9.73, 9.94	14.98, 15.1, 15.96, 16.11
7	15.98, 16.11, 17.28, 17.56	21.23, 22.33, 26.33, 27.86	8.68, 8.98, 9.65, 9.93	15.0, 15.19, 16.0, 16.19
8	15.96, 16.1, 17.32, 17.67	21.16, 22.58, 26.33, 27.42	8.59, 8.93, 9.69, 9.95	15.0, 15.16, 15.92, 16.11
9	15.93, 16.1, 17.41, 17.79	21.16, 22.45, 26.21, 27.49	8.84, 8.97, 9.63, 9.85	14.99, 15.1, 15.95, 16.12
10	15.89, 16.04, 17.53, 17.76	21.5, 22.38, 26.72, 28.26	8.78, 9.02, 9.69, 9.95	15.07, 15.15, 15.94, 16.13
11	15.93, 16.19, 17.43, 17.8	21.42, 22.26, 26.83, 27.88	8.65, 8.97, 9.65, 9.81	15.1, 15.26, 16.03, 16.21
12	-	-	8.44, 8.64, 10.07, 10.21	15.01, 15.09, 16.3, 16.64
13	-	-	8.9, 9.08, 9.98, 10.17	15.19, 15.34, 16.41, 16.72
14	15.9, 16.04, 17.29, 17.5	21.29, 22.2, 26.6, 27.87	8.6, 8.94, 9.67, 9.78	14.96, 15.09, 15.93, 16.13
15	-	-	8.56, 8.85, 9.97, 10.14	15.16, 15.26, 16.72, 17.01
16	-	22.63, 23.09, 28.08, 28.23	8.66, 9.16, 10.03, 10.41	15.27, 15.46, 16.32, 16.67
17	14.86, 15.44, 17.22, 17.77	20.9, 21.98, 26.1, 27.3	-	-
18	15.95, 16.06, 17.38, 17.9	21.48, 22.51, 26.4, 27.16	-	14.85, 15.1, 15.95, 16.15
19	15.91, 16.11, 17.35, 17.84	21.73, 22.46, 26.55, 27.17	8.87, 9.06, 9.71, 9.87	14.86, 15.15, 15.96, 16.14
20	15.92, 16.12, 17.37, 17.72	21.39, 22.46, 26.5, 27.74	8.79, 8.99, 9.73, 9.84	14.9, 15.06, 16.03, 16.17
21	-	-	8.5, 8.78, 9.62, 10.0	14.71, 14.97, 15.97, 16.39
22	-	-	8.86, 9.02, 10.05, 10.23	15.13, 15.39, 16.5, 16.79
23	-	-	8.76, 9.01, 9.79, 10.05	14.8, 15.14, 16.22, 16.77
24	-	-	8.74, 8.93, 10.05, 10.24	15.11, 15.4, 16.44, 16.74
31	-	-	8.52, 8.87, 9.65, 9.76	14.89, 15.11, 15.79, 16.21
32	-	-	8.29, 8.84, 9.64, 9.78	14.92, 15.1, 15.96, 16.22
33	-	-	8.26, 8.84, 9.73, 9.87	14.86, 14.94, 15.86, 16.39
34	-	-	8.18, 8.74, 9.82, 10.14	14.94, 15.24, 16.2, 16.44
35	-	-	8.31, 8.69, 9.95, 10.13	15.04, 15.14, 16.03, 16.47
36	-	-	8.35, 8.68, 9.97, 10.12	15.14, 15.24, 16.2, 16.65
37	-	-	9.15, 9.25, 9.64, 9.71	15.45, 15.53, 16.52, 17.3
38	14.1, 15.27, 16.87, 17.45	20.98, 22.01, 25.6, 26.77	-	-
39	14.82, 15.43, 17.09, 17.64	21.5, 22.15, 25.64, 27.79	-	-
40	13.97, 15.38, 17.34, 18.0	20.92, 21.97, 26.23, 27.62	-	-
41	14.84, 15.8, 17.5, 18.0	21.3, 22.25, 26.58, 27.38	-	-
42	14.97, 15.88, 17.83, 18.51	23.77, 24.44, 27.44, 28.57	-	-
43	15.54, 16.46, 18.12, 18.63	-	-	-
44	15.61, 16.49, 18.35, 18.76	-	-	-
45	15.49, 16.6, 18.6, 19.12	-	-	-
46	13.9, 15.25, 16.91, 17.43	21.2, 21.92, 24.22, 24.6	-	-
47	14.12, 15.12, 16.99, 17.43	21.5, 21.82, 24.34, 24.85	-	-
48	14.39, 15.24, 17.0, 17.54	21.26, 21.77, 24.59, 25.15	-	-
49	13.86, 15.27, 17.02, 17.59	21.34, 21.89, 24.59, 24.96	-	-
50	14.35, 15.29, 17.1, 17.5	21.26, 22.2, 24.49, 24.82	-	-
51	13.52, 14.88, 17.19, 17.59	21.09, 21.97, 24.45, 24.84	-	-
52	-	-	8.33, 8.78, 9.51, 10.05	14.6, 15.01, 15.74, 16.1
53	-	-	8.75, 8.89, 9.48, 9.73	14.6, 15.0, 15.74, 16.06
54	-	-	8.74, 8.93, 9.5, 9.76	14.6, 15.02, 15.8, 16.44
55	-	-	8.79, 8.9, 9.48, 9.65	14.74, 15.02, 15.93, 16.28
56	-	-	-	-
57	-	-	-	-
58	-	-	-	-
59	-	-	-	-
60	-	-	-	-

Table 7: Spectral feature continua points. Part 2

#	16 μm band	24 μm band	9 μm band	15 μm band
61	-	-	-	-
62	-	-	-	-
63	-	-	-	-
64	15.53, 15.92, 17.15, 17.68	-	-	-
65	15.53, 15.78, 17.05, 17.46	22.65, 23.15, 24.45, 24.99	-	-
66	15.83, 16.02, 16.74, 17.11	21.87, 22.37, 24.56, 24.9	8.77, 8.9, 9.64, 9.8	14.85, 15.04, 15.84, 16.07
67	14.96, 15.58, 17.65, 18.29	22.48, 22.95, 24.63, 24.95	-	-
68	15.8, 15.99, 17.02, 17.3	-	-	14.66, 14.82, 15.89, 16.11
69	-	21.92, 22.63, 25.27, 26.12	8.84, 9.02, 9.65, 9.73	-
70	15.52, 15.84, 16.74, 17.25	-	-	14.94, 15.03, 15.7, 15.91
71	15.43, 15.68, 17.03, 17.34	21.29, 22.24, 24.58, 24.88	8.79, 8.96, 9.56, 9.69	14.9, 15.07, 15.85, 16.08
72	-	21.76, 22.4, 24.78, 26.04	8.43, 8.89, 9.67, 9.73	-
73	15.63, 15.97, 16.8, 17.09	-	-	-
74	-	-	-	-
75	-	-	-	-
76	-	-	-	-
77	15.39, 15.9, 17.73, 18.22	-	8.62, 8.94, 9.58, 9.71	-
78	15.54, 15.91, 16.69, 16.91	-	-	-
79	15.47, 15.82, 16.66, 16.87	-	-	-
80	15.37, 15.92, 16.99, 17.45	-	-	-
81	-	21.93, 22.53, 24.42, 24.94	8.78, 8.91, 9.57, 9.67	-
82	-	21.95, 22.62, 24.67, 24.99	8.73, 8.93, 9.58, 9.77	14.94, 15.11, 16.01, 16.12
83	-	-	-	-
84	-	-	-	-
85	-	-	-	-
86	15.62, 15.95, 17.92, 18.31	-	8.73, 8.88, 9.68, 9.81	14.78, 14.99, 15.86, 16.16
87	-	-	-	-
88	-	-	-	-
89	15.41, 15.84, 17.01, 17.63	-	-	-
90	15.43, 15.93, 17.8, 18.18	-	8.68, 8.98, 9.69, 9.78	-
91	15.01, 15.44, 17.44, 17.87	22.25, 22.61, 24.59, 25.08	8.79, 8.95, 9.56, 9.68	-
92	15.24, 15.5, 17.84, 18.07	-	8.65, 9.03, 9.63, 9.79	-
93	15.33, 15.71, 17.92, 18.32	-	8.72, 8.96, 9.61, 9.68	-
94	15.76, 15.94, 17.69, 17.98	-	8.7, 8.89, 9.58, 9.71	14.87, 15.01, 15.73, 15.94
95	14.8, 15.29, 17.22, 17.63	21.32, 21.84, 26.3, 26.7	-	-
96	15.04, 15.41, 17.28, 17.76	21.37, 22.01, 26.01, 26.62	8.6, 8.88, 9.55, 9.81	-
97	15.14, 15.3, 17.05, 17.42	21.51, 21.94, 26.03, 26.74	8.58, 8.87, 9.57, 9.72	-
98	14.55, 15.14, 17.25, 17.7	21.35, 21.91, 26.02, 26.73	-	-